Evaluation of near-singular integrals with application to vortex sheet flow

***Monika Nitsche**
Department of Mathematics and Statistics, University of New Mexico
Albuquerque, NM 87131, USA
nitsche@math.unm.edu

Communicated by

Received: date / Accepted: date

Abstract. This paper presents a method to evaluate the near-singular line integrals that solve elliptic boundary value problems in planar and axisymmetric geometries. The integrals are near-singular for target points not on, but near the boundary, and standard quadratures lose accuracy as the distance d to the boundary decreases. The method is based on Taylor series approximations of the integrands that capture the near-singular behaviour and can be integrated in closed form. It amounts to applying the trapezoid rule with meshsize h, and adding a correction for each of the basis functions in the Taylor series. The corrections are computed at a cost of $O(n_w)$ per target point, where typically, $n_w = 10 - 40$. Any desired order of accuracy can be achieved using the appropriate number of terms in the Taylor series expansions. Two explicit versions of order $O(h^2)$ and $O(h^3)$ are listed, with errors that decrease as $d \to 0$. The method is applied to compute planar potential flow past a plate and past two cylinders, as well as long-time vortex sheet separation in flow past an inclined plate. These flows illustrate the significant difficulties introduced by inaccurate evaluation of the near-singular integrals and their resolution by the proposed method. The corrected results converge at the analytically predicted rates.

1. Introduction

Interfacial flows in either inviscid fluid or highly viscous Stokes flow are efficiently described using a boundary integral representation of the governing elliptic partial differential equations. The fluid velocity at any target point is given by an integral along the interface in terms of a problem dependent Green's function and a density function. A sample interface could be a vortex sheet in inviscid flow, or the boundary of drops and bubbles in Stokes flow. The effect of solid walls in the fluid can be treated similarly. Numerical methods based on the resulting boundary integral equations (BIE) are efficient, as they reduce the problem to a lower-dimensional one, accurate, as they track the interface with high resolution, and flexible, as multiple domains and moving boundaries are easily addressed. The boundary integrals that appear are of three types. For target points on the boundary the integrals are singular. For target points far from the boundary the integrals are regular. In both of these cases they can be evaluated accurately using a range of existing methods. However, as is well-known, for target points not on the boundary but near it, the integrals are near-singular and standard quadrature rules lose accuracy. This issue is the subject of this paper.

An example illustrating the consequence of inaccuracies near the boundary is presented in figure 1. The figure shows a vortex sheet (in red) that has formed by the separation of vorticity at the edges of a plate inclined in a parallel background flow (in green). The sheet velocity is given by a boundary integral over

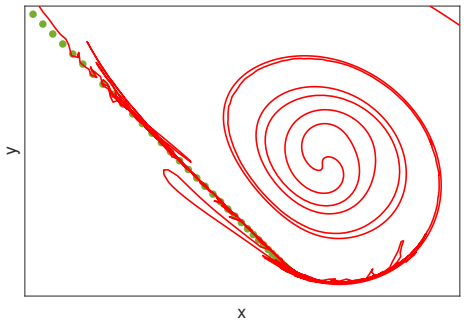

Figure 1. Sample simulation of vortex sheet separation (red) at the edge of a plate (green) showing the effect of inaccuracies when the vortex sheet is near the plate.

the plate, which is near-singular when the sheet is nearby. Inaccurate evaluation leads to unphysical vortex sheet crossing through the plate, after which the motion becomes highly irregular, as shown in the figure, and the computation quickly breaks down.

Accurate evaluation of the near-singular integrals has been the subject of much research, with early works such as of Mayo (1985), motivated by solutions to the Laplace, Helmholtz, or Stokes equations. By now, several accurate and fast algorithms have been developed for planar geometries, where the boundary integrals reduce to 1D line integrals. Ying, Biros and Zorin (2006) use interpolation of integral values on and far from the boundary to obtain the values near the boundary. Quaife and Biros (2014) applied this approach to planar Stokes flow. Beale and Lai (2001) regularize the near-singular integrands and add corrections obtained from asymptotic approximations. This approach was used by Cortez (2001) to compute regularized planar Stokes flow. Carvalho, Khatri and Kim (2018) used matched asymptotic expansions in the near-boundary region. Several highly accurate methods exploit the fact that for planar flows the integrals are given by analytic functions. Among these are the works of Helsing and Ojala (2008), who present an interpolatory panel method for Laplace's equation; Ojala and Tornberg (2015), who adapted this method to multiphase Stokes flow; and Barnett, Wu and Veerapaneni (2015), who present a method based on a baricentric formula for Cauchy integrals. Pérez-Arancibia, Faria and Turc (2019) recently proposed a method based on interpolating the density function. The Quadrature-By-Expansion (QBX) method developed by Klöckner *et al.* (2013), building on the work of Barnett (2014), is based on high order kernel expansions about interior domain points that are sufficiently far from the boundary that all integrals can be resolved accurately. This method has recently been generalized to generic kernels by Rahimian, Barnett and Zorin (2018).

In this paper we present a method based on Taylor series approximations of the integrands about points on the boundary. This idea is novel although many connections with earlier works exist (see below). This work originated from the author's study of multi-drop axisymmetric Stokes flow. There, inaccuracies near the drop interfaces lead to drop boundary crossings and subsequent break-down of the solution. The line integrals arising in axisymmetric geometry are not analytic and many of the existing methods cannot be applied. As a result we have developed a simple method for a range of 1D integrals, including those in axisymmetric geometry. It is fully understood analytically and can be formulated to satisfy any prescribed order of accuracy. This paper introduces the method and the analytical results, and, to illustrate, applies it to vortex sheet flow such as presented in figure 1, where the integrals are most simple. The method has also been applied to axisymmetric Stokes flow, although the details in that case are more complex and will be presented elsewhere. The remainder of this introduction describes the problem to be solved, outlines the method and presents its relation to prior as well as outstanding work.

The problem. Of interest here is the numerical evaluation of near-singular line integrals of the form,

$$\int_a^b \frac{F(\mathbf{x}(\alpha),\mathbf{x}_0)}{|\mathbf{x}(\alpha)-\mathbf{x}_0|^p}\,\omega(\alpha)\,d\alpha\ , \qquad \int_a^b \log|\mathbf{x}(\alpha)-\mathbf{x}_0|^2\,\omega(\alpha)\,d\alpha. \tag{1}$$

for any integer values p for which the integrand is integrable in the principal value sense. Here $\mathbf{x}(\alpha)$, $\alpha\in[a,b]$, is a smooth parametrization of a curve C in the plane. The function $F(\mathbf{x},\mathbf{x}_0)$ is given by a

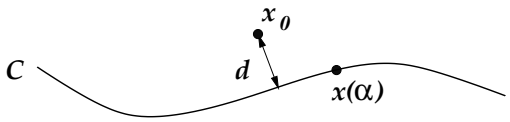

Figure 2. Sketch showing curve C given by $\mathbf{x}(\alpha)$ with target point $\mathbf{x}_0$ at distance d from C.

problem dependent kernel, $\omega(\alpha)$ is the density, and both are assumed to be smooth for target points $\mathbf{x}_0$ not on the curve C, but at a distance d, as illustrated in figure 2. The near-singular case corresponds to small d.

In planar vortex sheet flow, the integrals are of this form with $p = 2$. In axisymmetric flow, $p = 2, 3, 4$ occur. The results in this paper apply to all such integrals, although the focus is on $p = 2, 4$ and the logarithm. It is important to note that since these integrals stem from boundary integral formulations, they are integrable in at least the principal value sense when $\mathbf{x}_0 \in C$. Thus, for $p > 1$, the functions F encountered in applications must have roots $\mathbf{x} = \mathbf{x}_0$ of sufficient multiplicity for integrability. For example, if $p = 2$, F must have a simple root, while for $p = 4$, it must have a triple root.

The method. The method consists of approximating the integrand by a function that captures the near-singular behaviour and can be integrated analytically. The approximation is obtained using Taylor series expansions of $\mathbf{x}(\alpha)$ and $\omega(\alpha)$ about a point $\alpha = \alpha_p$ on the boundary. It consists of a sum of elementary basis functions. A correction is computed for each of the basis functions and added to a basic 4th-order Trapezoid approximation of the integral using a uniform mesh of size h.

The correction consists of integrating the basis functions exactly over an interval of $2n_w$ gridpoints centered near α_p, at a cost of $O(n_w)$ per target point, where typically, $n_w = 10 - 40$. The number of basis functions depends on the desired order of accuracy. As examples, we present $O(h^2)$ and $O(h^3)$ versions for $p = 2, 4$, and the logarithm. We also show that the approximation is increasingly accurate as $d \to 0$, to within an $O(h^4)$ term, limited by machine precision. Arbitrarily higher order versions can be obtained for any p using analytical convergence results for each basis function. The method is conceptually simple, simple to implement, and accurate near the boundary. It relies solely on the expressions for F and ω, and is therefore not restricted to planar geometries. The method does not depend on the trapezoid rule, which could be replaced by any other quadrature of choice.

Vortex sheet flow. We apply the method to compute planar vortex sheet flows, including potential flow past a plate, flow past two cylinders, and vortex sheet separation at the edge of a plate in a background flow, where we include both leading and trailing edge separation. The potential flow examples provide good test cases since they clearly illustrate the main difficulties caused by inaccurate evaluation of the near-singular integrals. These difficulties are present in the more physical, and significantly more complex vortex sheet separation example. This latter flow is difficult to compute accurately, as shown in figure 1, since at all times the separated sheet has portions lying along the plate, arbitrarily close to it. An example where potential flow arises in a real physical situation is Hele-Shaw flow.

The fluid velocity in all planar vortex sheet flows is given by an integral of type (1) with $p = 2$, and the stream function has a logarithmic near-singularity. We compare results using the Trapezoid rule with and without corrections and show that the analytically predicted convergence rates are attained. The trapezoid rule is equivalent to the point vortex approximation of the sheet. The numerical method thus consists of adding corrections to the point vortex approximation whenever the target point $\mathbf{x}_0$ is close to the wall. It enables us to compute long-term simulations of vortex sheet separation past a plate. Similarly, the method can be directly applied to the vortex sheet calculations considered by Sohn (2020), Elling (2020), Darakananda *et al*. (2018) who have all reported difficulties with near-boundary simulations, as well others such as Alben (2015), Jones and Shelley (2005), Shukla and Eldredge (2007), Xu, Nitsche and Krasny (2017), where the near-boundary situation appears.

Relation to prior work. As mentioned, several methods have been proposed for near-singular line integrals in planar geometries. Out of these methods, those based on integrating analytic functions are the most simple

and accurate. While those methods are not directly applicable to the integrals of interest here, which are motivated by axisymmetric geometries and thus not analytic, there are similarities with the present work. Most closely, the present method is related to the work of Helsing and Ojala (2008), as well as that of Pérez-Arancibia, Faria and Turc (2019). In both of those works, approximate integrands are integrated exactly. There, the approximations are obtained by interpolation. Here, they are obtained by Taylor series. That is a different approach than for example that of Khatri *et al*. (2020), who approximate the integral instead of the integrand. Similar to the QBX method (Epstein, Greengard and Klöckner (2013); Klinteberg and Tornberg (2017, 2018); Siegel and Tornberg (2018)), or the regularization method of Beale and coworkers (Beale and Lai (2001); Tlupova and Beale (2013); Beale, Ying and Wilson (2016); Tlupova and Beale (2019)), the proposed method is presented with a solid convergence theory. Finally, we note that many of the earlier results have been applied to Stokes flow. The application considered here is in a sense more singular, since vortex sheet flow is discontinuous across interfaces which is not the case in Stokes flow. The present application may thus present a more stringent test case.

However, the problem of biggest current interest is to apply what has been learned for line integrals to find efficient methods for surface integrals that occur in fully 3D geometries. Several approaches have been extended to 3D including the interpolation method of Ying, Biros and Zorin (2006), the QBX method (Siegel and Tornberg (2018); Klinteberg and Tornberg (2016)), the regularization method of Tlupova and Beale (2019), the density interpolation method of Pérez-Arancibia, Faria and Turc (2019), and Khatri *et al*. (2020)'s recent work using asymptotic approximations of integral quantities. The present approach, introduced here for 2D line integrals, presents an alternative based on Taylor series expansions that can in principle be generalized to 3D, and, in view of its simplicity and proven accuracy, may provide a competitive option. Furthermore, since the method consists of adding a correction to standard quadratures, it can easily be incorporated as a simple addition to existing vortex sheet codes. Thus, in summary, here we introduce a novel idea with proven convergence results, apply it to a class of problems not considered in prior related work, and provide a basis that can potentially be extended to 3D.

Organization of the paper. The paper is organized as follows. Section 2 describes the method and outlines the derivation of the associated convergence rates. Section 3 applies the method to several examples in vortex sheet flow and confirms the analytically predicted results. In Section 4, we derive the key ingredient needed to prove convergence. The work is summarized in section 5.

2. Numerical Method

We consider integrals of form (1) for small values of d. The curve C, its parametrizaton $\mathbf{x}(\alpha)$, and the functions F, ω are all assumed to be smooth. Section 2.1 presents a simple example that illustrates the difficulties in evaluating these integrals and motivates the proposed method. Sections 2.2-2.5 describe the method and how to obtain convergence of arbitrary order, and §2.6 discusses the effect of the window size n_w.

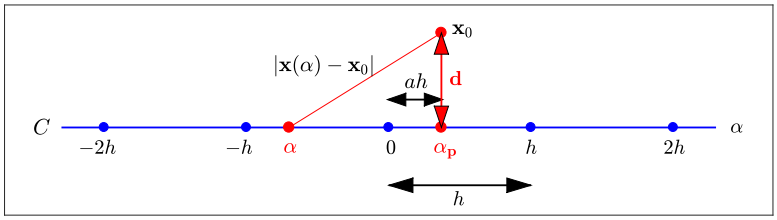

Figure 3. Motivating example. Flat curve C given by $\mathbf{x}(\alpha) = \alpha$, discretized by equally spaced points $\alpha_k = kh$. The point α_p is the orthogonal projection onto the curve of the point $\mathbf{x}_0$ at distance d. The distance from α_p to the closest gridpoint is measured by ah.

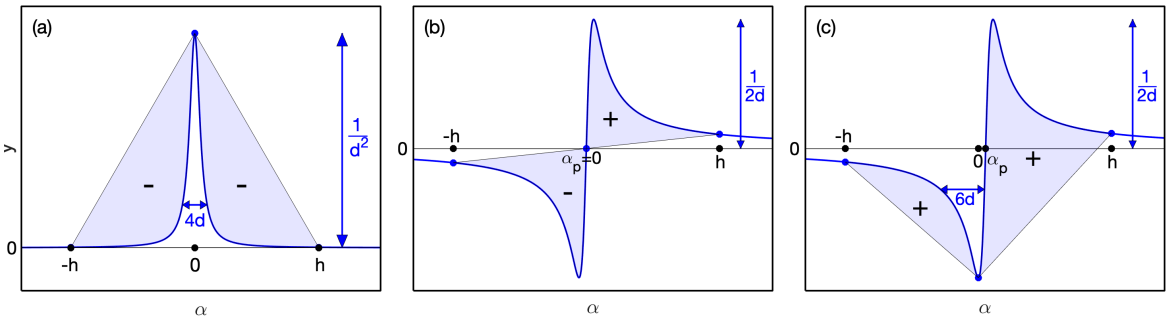

Figure 4. Graphs of (a) f_1 with $\alpha_p = 0$, (b) f_2 with $\alpha_p = 0$ and (c), f_2 with $\alpha_p > 0$, for $d \ll h$. The shaded area represents the error $E[f]$ on the interval $[-h, h]$. The sign of the the error on each piece is denoted by "-" and "+".

2.1. Motivating example

Consider a flat curve C given by $\mathbf{x}(\alpha) = (\alpha, 0)$, uniformly discretized by points $\alpha_k = kh$, and a target point $\mathbf{x}_0$ positioned near the origin with coordinates (α_p, d), as illustrated in figure 3. The projection α_p is at a distance ah from the nearest gridpoint. Now consider the error made by the trapezoid rule in evaluating the integral (1) with $p = 2$,

$$\int_I \frac{F(\mathbf{x}(\alpha), \mathbf{x}_0)}{|\mathbf{x}(\alpha) - \mathbf{x}_0|^2}\, d\alpha \tag{2}$$

over a small interval $I = [-h, h]$, for simple numerators $F = 1$ or $F = \alpha - \alpha_p$. Since $|\mathbf{x}(\alpha) - \mathbf{x}_0|^2 = d^2 + (\alpha - \alpha_p)^2$, the integrands reduce to

$$f_1(\alpha) = \frac{1}{d^2 + (\alpha - \alpha_p)^2} \quad \text{or} \quad f_2(\alpha) = \frac{\alpha - \alpha_p}{d^2 + (\alpha - \alpha_p)^2}\ . \tag{3}$$

Figure 4(a) plots $f_1(\alpha)$ for a generic value of $d \ll h$, and $\alpha_p = 0$. Two characteristic length scales are shown: the maximum value $1/d^2$, and a characteristic width $4d$ of the region where $f_1 \geq 1/(5d^2)$. These length scales indicate the behaviour of the graph as $d \to 0$. The shaded area represents the trapezoid rule error over the interval I,

$$E[f] = \int_I f - T[f]\ , \quad T[f] = \frac{h}{2}[f(-h) + 2f(0) + f(h)] \tag{4}$$

where the minus signs indicate that the contribution of each area is negative. It is clear from the figure that if $d \ll h$, the error equals the area of two almost triangular regions, but with negative sign,

$$E[f_1] \approx -h/d^2\ .$$

The absolute error thus tends to infinity as $d \to 0$, for any fixed meshsize h.

For f_2 the situation is slightly different. The function f_2 is odd about α_p and one may think that the trapezoid error is zero by cancellation. This is so if $\alpha_p = 0$, shown in figure 4(b),

$$E[f_2] = 0 \ \text{ if } \ \alpha_p = 0\ .$$

However, it is not true if $\alpha_p \neq 0$. If $\alpha_p = d$, shown in figure 4(c), the function takes on its maximal magnitude of $1/(2d)$ at the middle gridpoint. The figure shows that as a result, the contributions of the shaded areas to the error are both positive, with no cancellation. It is furthermore easy to see that the shaded area to the right of α_p and above the axis approximately equals the white area to the left between the axis and the function. Thus the total shaded area approximately equals that of a triangle with height $1/(2d)$ and width $2h$. We deduce that for $d \ll h$, the trapezoid error

$$E[f_2] \approx h/(2d) \ \text{ if } \ \alpha_p = d\ ,$$

which also approaches infinity as $d \to 0$. Thus, in the case of f_2 the error oscillates greatly, between 0 and $h/(2d)$, as the target point $\mathbf{x}_0$ moves *at a constant distance* d parallel to the curve C. This illustrates the importance of the parameter ah shown in figure 3.

This simple scenario illustrates the difficulty in accurately evaluating the near-singular integrals using standard quadratures. However, it also motivates the method proposed next: the key idea is that functions of type f_1, f_2 are leading-order approximations to the integrands and can be integrated exactly.

2.2. The Method in a Nutshell

For concreteness, we focus on three types of integrals of form (1), with integrands

$$G_2(\alpha) = \frac{F_2(\mathbf{x}(\alpha), \mathbf{x}_0)}{|\mathbf{x}(\alpha) - \mathbf{x}_0|^4}\,\omega(\alpha)\ , \quad G_1(\alpha) = \frac{F_1(\mathbf{x}(\alpha), \mathbf{x}_0)}{|\mathbf{x}(\alpha) - \mathbf{x}_0|^2}\,\omega(\alpha)\ , \quad G_0(\alpha) = \log|\mathbf{x}(\alpha) - \mathbf{x}_0|^2\omega(\alpha). \tag{5}$$

corresponding to $p = 2, 4$ and the logarithm. The distance from $\mathbf{x}_0$ to the curve is d, and h is the meshsize of a uniform discretization $\{\alpha_k\}_{k=0}^n$ of $[a, b]$. The main idea is to approximate the near-singular functions $G(\alpha)$ to leading order for $d \ll h$ by a function $\mathcal{H}(\alpha)$ that captures the near-singularity and can be integrated exactly. We then approximate the integral of G as follows:

$$\int G = \int (G - \mathcal{H} + \mathcal{H}) \tag{6a}$$

$$\approx T_4[G - \mathcal{H}] + \int \mathcal{H} \tag{6b}$$

$$= T_4[G] + \Big(\int \mathcal{H} - T_4[\mathcal{H}] \Big) \tag{6c}$$

$$= T_4[G] + E_4[\mathcal{H}]\ . \tag{6d}$$

In (6a), we add and subtract the approximation from G. In (6b), we approximate the smoother difference $G - \mathcal{H}$ by a fourth order generalized trapezoid rule T_4, while integrating $\mathcal{H}$ exactly. This step represents the main improvement in approximating $\int G$, since the more egregious over/under predictions of the trapezoidal rule on G are essentially removed by applying the same approximation to $\mathcal{H}$. We proceed to rewrite expression (6b) by rearranging the terms using the linearity of T_4 (6c), yielding the final expression (6d). This expression summarizes the method as implemented: it consists of adding the correction $E_4[\mathcal{H}] = \int \mathcal{H} - T_4[\mathcal{H}]$ to the trapezoid approximation of the uncorrected integral. This has the advantage that $T_4[G]$ can be computed first for all target points $\mathbf{x}_0$ of interest, and the correction $E_4[\mathcal{H}]$ can then be added only to those points that are too close to the curve C. In this form, the correction is easily added to existing codes in which $T_4[G]$ is already computed.

For T_4 we use

$$T_4[f] = h{\sum_{k=0}^{n}}' f(\alpha_k) - \frac{h^2}{12}[f'(b) - f'(a)]\ , \tag{7}$$

where the prime on the summation denotes that the first and last term in the sum are weighted by 1/2. As a result the pointwise convergence for any fixed target point $\mathbf{x}_0$ is $O(h^4)$.

Typically, we do not compute the correction $E_4[\mathcal{H}]$ over the whole domain, but only over a small domain consisting of $2n_w$ gridpoints approximately centered on α_p. The cost of computing the correction is $O(n_w)$. The effect of the window size n_w is addressed below, in §2.6.

This basic approach follows that of earlier work by the author and coworkers in Nitsche (1999, 2001); Nitsche *et al.* (2010). There, it was used to evaluate singular integrals in axisymmetric Stokes and vortex sheet flow for target points on the interface, near the axis of symmetry.

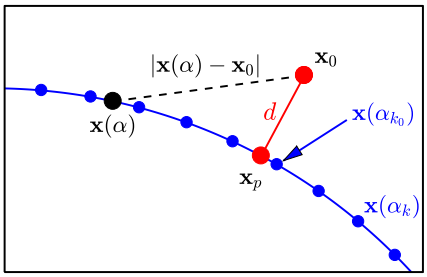

Figure 5. Projection $\mathbf{x}_p = \mathbf{x}(\alpha_p)$ of $\mathbf{x}_0$ onto curve given by $\mathbf{x}(\alpha)$, which is discretized by points $\mathbf{x}(\alpha_k)$. The point $\mathbf{x}(\alpha_{k_0})$ is the gridpoint closest to $\mathbf{x}_p$.

2.3. The approximation $\mathcal{H}$

We begin by finding the orthogonal projection $\mathbf{x}_p = \mathbf{x}(\alpha_p)$ of $\mathbf{x}_0$ onto the curve C (see figure 5). This step determines $d = |\mathbf{x}_0 - \mathbf{x}_p|$ and the basepoint α_p. The approximation $\mathcal{H}$ consists of a Taylor approximation of $G(\alpha)$ about α_p. It is obtained by expanding both the numerator and the denominator of G using as many terms as needed for the desired accuracy, applying the geometric series, and truncating the result. The number of required terms is addressed in §2.4 and follows from convergence results derived in §4.

The expansion of the denominator, given here to 5th order, is,

$$\begin{aligned} |\mathbf{x}(\alpha) - \mathbf{x}_0|^2 =& [\ (\mathbf{x}_p - \mathbf{x}_0) + \dot{\mathbf{x}}_p(\alpha-\alpha_p) + \frac{1}{2}\ddot{\mathbf{x}}_p(\alpha-\alpha_p)^2 + \frac{1}{6}\dddot{\mathbf{x}}_p(\alpha-\alpha_p)^3 + O((\alpha-\alpha_p)^4\ ]\cdot \\ & [\ (\mathbf{x}_p - \mathbf{x}_0) + \dot{\mathbf{x}}_p(\alpha-\alpha_p) + \frac{1}{2}\ddot{\mathbf{x}}_p(\alpha-\alpha_p)^2 + \frac{1}{6}\dddot{\mathbf{x}}_p(\alpha-\alpha_p)^3 + O((\alpha-\alpha_p)^4\ ] \\ =& d^2 + c^2(\alpha-\alpha_p)^2 + e_3(\alpha-\alpha_p)^3 + e_4(\alpha-\alpha_p)^4 + O((\alpha-\alpha_p)^5)\ , \end{aligned} \tag{8}$$

where

$$c^2 = |\dot{\mathbf{x}}_p|^2 + \ddot{\mathbf{x}}_p \cdot (\mathbf{x}_p - \mathbf{x}_0), \tag{9a}$$

$$e_3 = \dot{\mathbf{x}}_p \cdot \ddot{\mathbf{x}}_p + \frac{1}{3}(\mathbf{x}_p - \mathbf{x}_0)\cdot \dddot{\mathbf{x}}_p = \tilde{e}_3 + O(d), \tag{9b}$$

$$e_4 = \tilde{e_4} + O(d), \tag{9c}$$

with (9d)

$$\tilde{e}_3 = \dot{\mathbf{x}}_p \cdot \ddot{\mathbf{x}}_p, \tag{9e}$$

$$\tilde{e}_4 = \dot{\mathbf{x}}_p \cdot \dddot{\mathbf{x}}_p/3 + \ddot{\mathbf{x}}_p \cdot \ddot{\mathbf{x}}_p/4, \tag{9f}$$

and $\dot{\mathbf{x}}_p = \dot{\mathbf{x}}(\alpha_p)$, $\ddot{\mathbf{x}}_p = \ddot{\mathbf{x}}(\alpha_p)$, $\dddot{\mathbf{x}}_p = \dddot{\mathbf{x}}(\alpha_p)$.

The constant term in the expansion given in (8) is simply the distance d squared. A linear term $\alpha - \alpha_p$ does not appear since $\mathbf{x}_p$ is defined to be the orthogonal projection of $\mathbf{x}_0$ onto the sheet, and $\dot{\mathbf{x}}_p$ is tangent to the sheet, so that $\dot{\mathbf{x}}_p \cdot (\mathbf{x}_p - \mathbf{x}_0) = 0$. It is not necessary to ensure that the linear term vanishes, but it simplifies the resulting expressions for $\mathcal{H}$ given below, obtained by truncating the above expansion, and thereby simplifies the corresponding integral $\int \mathcal{H}$. In addition, in the presence of a linear term one must be careful to avoid division by zero that can occur after truncation. In general, finding the orthogonal projection accurately is easy (see details given in §2.5) and no advantage has been found to considering the more general inclusion of a linear term.

The quadratic term $(\alpha-\alpha_p)^2$ is multiplied by the constant c^2. The results in this paper assume that c^2 is strictly bounded away from zero. For the examples considered in §3, c^2 is positive. In particular, as shown in Appendix A, c^2 is always positive if C is flat or if $\mathbf{x}_0$ lies on the "outside" of a curve that is uniformly discretized in arclength. If it lies "inside", $c^2 > 0$ when d is less than the radius of the osculating circle at $\mathbf{x}_p$, R_{osc}. Here, the inside is defined to be the side of the osculating circle. The constant c^2 is strictly bounded away from zero when d is strictly less than R_{osc}.

The quantities $\tilde{e}_3$ and $\tilde{e}_4$ denote the dominant terms of the coefficients e_3 and e_4 of the cubic and quartic terms, respectively. Note that they depend on fewer derivatives of the curve $\mathbf{x}(\alpha)$ at α_p than e_3 and e_4: $\tilde{e}_3$ depends on 2 derivatives, $\tilde{e}_4$ depends on 3.

Now we use a Taylor expansion of the numerator and the geometric series to obtain a series approximation for G. The approximations $\mathcal{H}$ are obtained by truncating that series. To illustrate, the expansion of G_1 and its approximation $\mathcal{H}_{11}$ are given next, where, for convenience, $\hat{\alpha} = \alpha - \alpha_p$,

$$G_1(\alpha) = \frac{F_1(\mathbf{x}(\alpha), \mathbf{x}_0)}{|\mathbf{x}(\alpha) - \mathbf{x}_0|^2}\,\omega(\alpha) = \frac{c_0 + c_1\hat{\alpha} + c_2\hat{\alpha}^2 + O(\hat{\alpha}^3)}{d^2 + c^2\hat{\alpha}^2 + e_3\hat{\alpha}^3 + O(\hat{\alpha}^4)} \tag{10a}$$

$$= \frac{c_0 + c_1\hat{\alpha} + c_2\hat{\alpha}^2 + O(\hat{\alpha}^3)}{d^2 + c^2\hat{\alpha}^2}\Big[1 - \frac{e_3\hat{\alpha}^3 + O(\hat{\alpha}^4)}{d^2 + c^2\hat{\alpha}^2}\Big] \tag{10b}$$

$$\approx \mathcal{H}_{11}(\alpha) = \frac{c_0 + c_1\hat{\alpha} + c_2\hat{\alpha}^2}{d^2 + c^2\hat{\alpha}^2} - \tilde{e}_3\frac{c_0\hat{\alpha}^3 + c_1\hat{\alpha}^4}{(d^2 + c^2\hat{\alpha}^2)^2}\ . \tag{10c}$$

Note that the geometric series expansion applied in step (10b) converges for sufficiently small $\hat{\alpha}$ since, even though $\hat{\alpha}^3$ is not necessarily smaller than d^2, $\hat{\alpha}^3$ is certainly smaller than $\hat{\alpha}^2$.

G_1	$\dfrac{F_1(\mathbf{x}(\alpha),\mathbf{x}_0)}{\lvert\mathbf{x}(\alpha)-\mathbf{x}_0\rvert^2}\,\omega(\alpha) = \dfrac{c_0+c_1\hat\alpha+c_2\hat\alpha^2+c_3\hat\alpha^3+O(\hat\alpha^4)}{d^2+c^2\hat\alpha^2+e_3\hat\alpha^3+e_4\hat\alpha^4+O(\hat\alpha^5)}$
$\mathcal{H}_{11}$	$\approx \dfrac{c_0+c_1\hat\alpha+c_2\hat\alpha^2}{d^2+c^2\hat\alpha^2} - e_3\dfrac{c_0\hat\alpha^3+c_1\hat\alpha^4}{(d^2+c^2\hat\alpha^2)^2}$
$\mathcal{H}_{12}$	$+\dfrac{c_3\hat\alpha^3}{d^2+c^2\hat\alpha^2} - \tilde e_3\dfrac{c_2\hat\alpha^5}{(d^2+c^2\hat\alpha^2)^2} - \tilde e_4\dfrac{c_0\hat\alpha^4+c_1\hat\alpha^5}{(d^2+c^2\hat\alpha^2)^2} + \tilde e_3^2\dfrac{c_0\hat\alpha^6+c_1\hat\alpha^7}{(d^2+c^2\hat\alpha^2)^3}$
G_2	$\dfrac{F_2(\mathbf{x}(\alpha),\mathbf{x}_0)}{\lvert\mathbf{x}(\alpha)-\mathbf{x}_0\rvert^4}\,\omega(\alpha) = \dfrac{c_0+c_1\hat\alpha+c_2\hat\alpha^2+c_3\hat\alpha^3+c_4\hat\alpha^4+c_5\hat\alpha^5+O(\hat\alpha^6)}{(d^2+c^2\hat\alpha^2+e_3\hat\alpha^3+e_4\hat\alpha^4+O(\hat\alpha^5))^2}$
	$= \dfrac{c_0+c_1\hat\alpha+c_2\hat\alpha^2+c_3\hat\alpha^3+c_4\hat\alpha^4+O(\hat\alpha^5)}{(d^2+c^2\hat\alpha^2)^2}\Big[1-2\dfrac{e_3\hat\alpha^3+O(\hat\alpha^4)}{d^2+c^2\hat\alpha^2}+\dfrac{O(\hat\alpha^6)}{(d^2+c^2\hat\alpha^2)^2}\Big]$
$\mathcal{H}_{21}$	$\approx \dfrac{c_0+c_1\hat\alpha+c_2\hat\alpha^2+c_3\hat\alpha^3+c_4\hat\alpha^4}{(d^2+c^2\hat\alpha^2)^2} - 2e_3\dfrac{c_0\alpha^3+c_1\hat\alpha^4+c_2\hat\alpha^5+c_3\hat\alpha^6}{(d^2+c^2\hat\alpha^2)^3}$
$\mathcal{H}_{22}$	$-2\tilde e_3\dfrac{c_4\hat\alpha^7}{(d^2+c^2\hat\alpha^2)^3} - 2\tilde e_4\dfrac{(c_0+c_1\hat\alpha+c_2\hat\alpha^2+c_3\hat\alpha^3)\hat\alpha^4}{(d^2+c^2\hat\alpha^2)^3}$
	$+\dfrac{c_5\hat\alpha^5}{(d^2+c^2\hat\alpha^2)^2} + 3\tilde e_3^2\dfrac{(c_0+c_1\hat\alpha+c_2\hat\alpha^2+c_3\hat\alpha^3)\hat\alpha^6}{(d^2+c^2\hat\alpha^2)^4}$
G_0	$\omega(\alpha)\log\lvert\mathbf{x}(\alpha)-\mathbf{x}_0\rvert^2 = \big[c_0+c_1\hat\alpha+c_2\hat\alpha^2+O(\hat\alpha^3)\big]\,\log\big(d^2+c^2\hat\alpha^2+e_3\hat\alpha^3+O(\hat\alpha^4)\big)$
	$= \big[c_0+c_1\hat\alpha+c_2\hat\alpha^2+O(\hat\alpha^3)\big]\big[\log(d^2+c^2\hat\alpha^2)+\dfrac{e_3\hat\alpha^3+O(\hat\alpha^4)}{d^2+c^2\hat\alpha^2}+\dfrac{O(\hat\alpha^6)}{(d^2+c^2\hat\alpha^2)^2}\big]$
$\mathcal{H}_{01}$	$\approx c_0\log(d^2+c^2\hat\alpha^2)$
$\mathcal{H}_{02}$	$+c_1\hat\alpha\log(d^2+c^2\hat\alpha^2)+\tilde e_3\dfrac{c_0\hat\alpha^3}{d^2+c^2\hat\alpha^2}$

Table 1. Summary of the approximations $G_j \approx \mathcal{H}_{j1}+\mathcal{H}_{j2}$. In each case, the approximations $G_j \approx \mathcal{H}_{j1}$ and $G_j \approx \mathcal{H}_{j1}+\mathcal{H}_{j1}$ yield an $O(h^2)$ and $O(h^3)$ approximations of $\int G_j$, respectively. For the $O(h^2)$ method, it is sufficient to replace e_3 by its dominant term $\tilde e_3$ in $\mathcal{H}_{j1}$. Throughout, $\hat\alpha = \alpha-\alpha_p$.

The approximation $G_1 \approx \mathcal{H}_{11}$ will be shown to yield a method of order $O(h^2)$. Alternatively, we can obtain an $O(h^3)$ method by keeping more terms in the series representation of G_1. For reference, all the terms of G_1, G_2, G_0 needed to obtain an $O(h^2)$ and an $O(h^3)$ method are tabulated in Table 1. The table rewrites each integrand as a sum $G_j \approx H_{j1}+\mathcal{H}_{j2}$, where H_{j1} and H_{j2} are as indicated. In each case, $G_j \approx \mathcal{H}_{j1}$ yields an $O(h^2)$ method, and the inclusion of more terms, using $G_j \approx \mathcal{H}_{j1}+\mathcal{H}_{j2}$, yields an $O(h^3)$ method to compute $\int G_j$. For all $O(h^2)$ methods, the coefficient e_3 in $\mathcal{H}_{j1}$ can be replaced by its dominant term $\tilde e_3$, as in (10c). These results follow from convergence results outlined next in §2.4 and derived in §4.

All approximations $\mathcal{H}$ of G given in Table 1 consist of a linear combination of basis functions of the form

$$H_{0k} = \hat\alpha^k\log(d^2+c^2\hat\alpha^2)\ , \quad H_{jk} = \frac{\hat\alpha^k}{(d^2+c^2\hat\alpha^2)^j}\ , \quad j\ge 1, k\ge 0 \tag{11}$$

The key is that all these basis functions can be integrated analytically in closed form, and thus the correction $E_4[\mathcal{H}]$ can be readily computed.

2.4. Convergence rates

What determines the number of terms used in the truncated Taylor series expansions needed to obtain a desired rate of convergence? The answer follows, firstly, from the bounds on the integration error of the

basis functions, $E_4[H_{jk}]$, as $d \to 0$. Following arguments similar to those in §2.1, one obtains the following results,

$$E_4[H_{jk}] = E_4\left[\frac{\hat{\alpha}^k}{(d^2+\hat{\alpha}^2)^j}\right] = O(hd^{k-2j}) \ , \tag{12a}$$

$$E_4[H_{0k}] = E_4[\,\hat{\alpha}^k \log(d^2+\hat{\alpha}^2)\,] = \begin{cases} O(h\log d) \ , & \text{if } k=0, \\ O(h^{k+1}) \ , & \text{if } k>0 \end{cases} \tag{12b}$$

in addition to an $O(h^4)$ term (or $O(h^4 \log h)$ for $j=0$) if $k \geq 2j+4$. Details of the derivation of (12) are given in §4.

Secondly, we use the fact that F_1 must have a simple root at $\mathbf{x}=\mathbf{x}_0$ which implies that, for F_1, $c_0 = O(d)$. Similarly, F_2 must have a triple root at $\mathbf{x}=\mathbf{x}_0$ and thus, for F_2, $c_0 = O(d^3)$, $c_1 = O(d^2)$, and $c_2 = O(d)$. As a result we can order the terms in the Taylor series expansion of G. For G_1, presented here as an example,

$$\begin{aligned} G_1(\alpha) = & \underbrace{\frac{c_0+c_1\hat{\alpha}}{d^2+c^2\hat{\alpha}^2}}_{E_4[\cdot]=O(h/d)} + \underbrace{\frac{c_2\hat{\alpha}^2}{d^2+c^2\hat{\alpha}^2} - e_3\frac{c_0\hat{\alpha}^3+c_1\hat{\alpha}^4}{(d^2+c^2\hat{\alpha}^2)^2}}_{E_4[\cdot]=O(h)} \\ & + \underbrace{\frac{c_3\hat{\alpha}^3}{d^2+c^2\hat{\alpha}^2} - e_3\frac{c_2\hat{\alpha}^5}{(d^2+c^2\hat{\alpha}^2)^2} - e_4\frac{c_0\hat{\alpha}^4+c_1\hat{\alpha}^5}{(d^2+c^2\hat{\alpha}^2)^2} + e_3^2\frac{c_0\hat{\alpha}^6+c_1\hat{\alpha}^7}{(d^2+c^2\hat{\alpha}^2)^3}}_{E_4[\cdot]=O(hd)} \\ & + \underbrace{\frac{O(\hat{\alpha}^4)}{d^2+c^2\hat{\alpha}^2} + \frac{O(d\hat{\alpha}^5,\hat{\alpha}^6)}{(d^2+c^2\hat{\alpha}^2)^2} + \frac{O(d\hat{\alpha}^7,\hat{\alpha}^8)}{(d^2+c^2\hat{\alpha}^2)^3} + \frac{O(d\hat{\alpha}^9,\hat{\alpha}^{10})}{(d^2+c^2\hat{\alpha}^2)^4}}_{E_4[\cdot]=O(hd^2,h^4)} \end{aligned} \tag{13}$$

The approximations $\mathcal{H}$ of G are then obtained by truncating the series. For example, the approximation $\mathcal{H}_{11}$ of G_1 consists of all terms whose integration error is bigger than $O(hd)$. Thus $E[G_1 - \mathcal{H}_{11}] = O(hd, h^4)$. Since the correction is only applied if $d = O(h)$, it follows that $E[G - \mathcal{H}_1] = O(h^2)$. Thus $G_1 \approx \mathcal{H}_{11}$ yields a second order method, with the additional property that the error vanishes as $d \to 0$, up to an $O(h^4)$ term. This $O(h^4)$ term is independent of d and of the distance ah from α_p to the nearest gridpoint (see figure 3).

The additional terms $\mathcal{H}_{12}$ in Table 1 consists of all terms whose integration error is $O(hd)$. Thus $E[G_1 - (\mathcal{H}_{11} + \mathcal{H}_{12})] = O(hd^2, h^4) = O(h^3)$. That is, the approximation $G_1 \approx \mathcal{H}_{11} + \mathcal{H}_{12}$ yields a third order method. The same criterion determines the number of terms used in the approximations of G_2 and G_0. With the information given in this section it becomes evident how to generalize the results to obtain a method of any desired order of accuracy.

A practical matter. An important consequence in practice regards the computation of the coefficients multiplying the basis functions. These coefficients depend on derivatives of F and ω at α_p. Consider the second order method given by $G_1 \approx \mathcal{H}_{11}$. The coefficient c_2 multiplies a term with integration error $O(h)$ and the correction by this term yields an overall error of $O(h^2)$. Thus c_2 needs to be evaluated only to order h. Similarly, c_1 needs to be evaluated to order h^2, etc, with the caveat that if the coefficients c_k are not computed more accurately, the approximation error loses the vanishing behaviour as $d \to 0$. In practice, we use finite difference approximations at the gridpoints (or spectral, when convenient) followed by interpolation to α_p.

Furthermore, since F_1 has a simple root at $\mathbf{x}=\mathbf{x}_0$, and thus $c_0 = O(d)$, it follows that the computation of c_0, c_1, c_2 requires second derivatives of the curve $\mathbf{x}(\alpha)$ at α_p, but only first derivatives of the density $\omega(\alpha)$. The same is true for the more singular function G_2: the triple root of F_2 implies that only second derivatives of $\mathbf{x}(\alpha)$ and first derivatives of $\omega(\alpha)$ are required to compute the 5 coefficients $c_0, \ldots, c_4$ needed for the $O(h^2)$ method. Similarly, 3 derivatives in $\mathbf{x}$ and 2 derivatives in ω are required for all $O(h^3)$ methods.

2.5. Implementation

For each G, the approximations $\mathcal{H}$ given in Table 1 are a sum of basis functions of the form (11). To compute the correction $E[\mathcal{H}]$ needed in (6d) we first compute $E[H_{jk}]$ for each required basis function. Moreover, it is only necessary to evaluate these errors over an interval approximately centered on α_p,

$$I = [\alpha_{k_0-n_w}, \alpha_{k_0+n_w}] \ . \tag{14}$$

where α_{k_0} is the closest gridpoint to α_p. Most results shown below use $n_w = 10$ although larger values are needed for higher accuracy as explained in §2.6.

These are the steps taken to implement the method, given here for the $O(h^2)$ version: for a given target point $\mathbf{x}_0$,

(1) Compute $T_4[G]$.
(2) If $\mathbf{x}_0$ is too close to C then
  (a) find $\alpha_p, d, \mathbf{x}_p, \dot{\mathbf{x}}_p, \ddot{\mathbf{x}}_p$ and $\omega'(\alpha_p)$
  (b) use the above to obtain $c, \tilde{e}_3$, and c_0, c_1, c_2 (for G_1, G_0) or c_0, c_1, c_2, c_3, c_4 (for G_2)
  (c) compute $E_4[H_{jk}]$ for all required basis functions (11) over the interval

$$I = [\alpha_{k_0-n_w}, \alpha_{k_0+n_w}] \ . \tag{15}$$

  where α_{k_0} is the closest gridpoint to α_p
  (d) correct $\displaystyle\int G \approx T_4[G] + \sum c'_{jk} E_4[H_{jk}]$ where c'_{jk} are the coefficients in the expansions (10c,12c,13c). The sum consists of 3, 5 and 9 terms for G_0, G_1 and G_2 respectively.

Several notes are in order:
(i) Definition of "too close": In the calculations in §3 below, the correction is applied when $d < 4\Delta s$, where Δs is the spacing between the two gridpoints closest to $\mathbf{x}_0$. This criterion is consistent with the one used by Klöckner *et al*. (2013), who considered the "high-accuracy region", in which standard quadratures give good results and no correction is necessary, to be at a distance of $5h \sim 5\Delta s$. That is the distance at which Klöckner *et al*. place the base points of their kernel expansions.
(ii) Finding α_p: In the examples below, the curve $\mathbf{x}(\alpha)$ is a prescribed flat or circular curve, and α_p can be found exactly with no computational cost. In general, for curves $\mathbf{x}(\alpha, t)$ that are not known except at the gridpoints, we first find the cubic interpolant through the four gridpoints closest to α_p, and then use Newton's method to find the value of α_p for which $\mathbf{x}(\alpha_p) - \mathbf{x}_0$ is normal to $\dot{\mathbf{x}}_p$. Very few Newton's iterations are sufficient.
(iii) In step 2ab: As noted before, the coefficients $c, \tilde{e}_3, c_0, c_1, c_2, c_3, c_4$ depend on up to second derivatives of the curve $\mathbf{x}(\alpha)$ and first derivatives of $\omega(\alpha)$ at α_p. These highest derivatives need to be computed to $O(h)$ only.
(iv) In step 2a: if $\mathbf{x}_0$ does not have an orthogonal projection onto C (for example, if it lies to the left or right of the flat plate considered below) yet is close enough to require correction, we use the closest point on C as $\mathbf{x}_p$. This does not introduce a linear term into (8), which would be given by $2\dot{\mathbf{x}}_p \cdot (\mathbf{x}_p - \mathbf{x}_0)(\alpha - \alpha_p)$, since we always impose $\dot{\mathbf{x}}_p = 0$ at tips. That is, we always cluster the points at least quadratically at the plate tip. Furthermore, $c^2 > 0$ in that case as well.
(v) In step 2c, for nonperiodic problems only: If α_p is too close to the endpoints of the interval of integration, $[a, b]$, it is possible that I does not lie within $[a, b]$. In that case we compute the corrections $E_4[H_{jk}]$ over the interval $I \cap [a, b]$.

2.6. Dependence on n_w

The bounds given in (12) estimate the integration error of H_{jk} over the interval I. This interval, denoted by $[a', b']$, and a generic basis function H are shown in figure 6. The method consists of removing these errors from $E_4[G]$ by integrating the near-singular H_{jk} exactly over I, while integrating them using T_4 over $[a, b] \setminus I = [a, a'] \cup [b', b]$. The error $E_4[H]$ over $[a, b] \setminus I$ is given by derivatives of the integrand at the

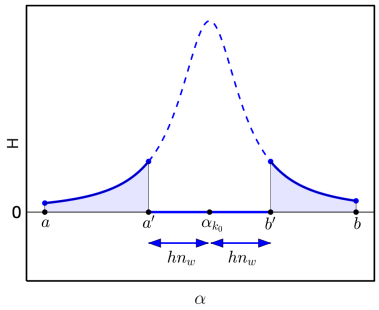

Figure 6. Sketch showing a generic basis function $H(\alpha)$, the interval $I = [a', b']$ over which it is integrated exactly, and the intervals $[a, a'] \cup [b', b]$ over which $\int H$ is approximated by the Trapezoid rule $T_4[H]$.

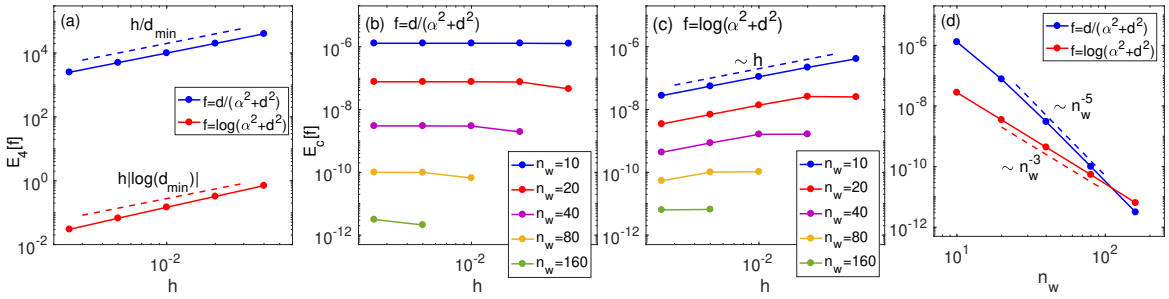

Figure 7. Errors in approximating $\int_a^b f$ where $[a, b] = [-1, 1]$, where f is as indicated. (a) Uncorrected error using T_4. (b,c) Corrected error using window of given size n_w, vs h, $h \in [0.0025, 0.04]$. (d) Corrected error for $h = 0.0025$ vs n_w. In all cases, the maximum error for $d \in [10^{-6}, 5h]$ is shown.

endpoints, following the Euler McLaurin formula. These derivatives are largest at a', b'. Thus we estimate, to leading order, $E_4[H] \approx \frac{h^4}{720}[H'''(a') - H'''(b')]$. Among the functions in the expansions in (10c-13c), this term is largest for

$$f_1(\alpha) = \frac{d}{d^2 + \hat{\alpha}^2} \ , \quad f_2(\alpha) = \log(d^2 + \hat{\alpha}^2) \ .$$

For these even functions, for small d, taken here to be $d \le 5h$, the error is approximated by

$$E[f_1] \approx 2|f_1'''(a')|\frac{h^4}{720} \approx \frac{d/h}{15n_w^5} \le \frac{1}{3n_w^5} \tag{16a}$$

$$E[f_2] \approx 2|f_2'''(a')|\frac{h^4}{720} \approx \frac{h}{90n_w^3} \tag{16b}$$

Figure 7 shows the maximal errors in integrating f_1 and f_2 over $[-1, 1]$, for $d \in [10^{-6}, 5h]$. Figure (a) plots the uncorrected error using T_4. The scaling of these uncorrected terms reflects the bounds given in (12). Figures (b-d) show the corrected errors using windows with the indicated values of n_w, and show agreement with the estimates (16) for the dependence on h and on n_w. Note that if $I \cap [a, b] = [a, b]$, there is no contribution from the endpoints as $a = a'$ and $b = b'$ so the error is zero, which explains the limited nonzero data for $n_w \ge 40$ in figures (b,c).

These figures show that while 10 digits of precision are gained using $n_w = 10$, larger windows should be used if higher precision is desired. While most results below are computed with $n_w = 10$, the effect of n_w was noticeable in the results presented in §3.1.2 below using the $O(h^3)$ method, which therefore were computed using $n_w = 20 - 80$. The contribution to the error by n_w depends on the quadrature rule used. It could be lowered using a different quadrature rule, such as a higher order trapezoid rule.

3. Vortex sheet flow

We now evaluate the performance of the method by applying it to test cases in vortex sheet flow such as those illustrated in figure 8: potential flow past objects (figures a,b,c) and vortex sheet separation at the edge of a plate in a background flow (figure d). In each case, the flow is induced by a vortex sheet bound to the object, shown in green, whose strength is such that the normal velocity on the boundary is zero. The velocity and streamfunction induced by the bound sheet C at a point $\mathbf{x}_0 \notin C$ are given by

$$\mathbf{u}(\mathbf{x}_0) = \frac{1}{2\pi}\int_a^b \frac{\mathbf{k}\times(\mathbf{x}-\mathbf{x}_0)}{|\mathbf{x}-\mathbf{x}_0|^2}\,\Gamma'(\alpha)\,d\alpha + \mathbf{U}_\infty\ , \tag{17a}$$

$$\psi(\mathbf{x}_0) = -\frac{1}{4\pi}\int_a^b \log|\mathbf{x}-\mathbf{x}_0|^2\,\Gamma'(\alpha)\,d\alpha + \psi_\infty\ , \tag{17b}$$

where $\mathbf{x}=\mathbf{x}(\alpha)$, $\alpha\in[a,b]$, is a parametrization of the sheet, the density $\Gamma'(\alpha)$ is the scaled sheet strength, $\mathbf{U}_\infty$ is the driving external flow and ψ_∞ the corresponding streamfunction. When $\mathbf{x}_0$ is near the boundary, these integrals are near-singular of the type discussed above. Note that in (17a), the single root of the numerator F_1 at $\mathbf{x}=\mathbf{x}_0$ is clearly evident.

In all cases, the scaled sheet strength Γ' is determined by no-through flow at the wall, $\mathbf{u}(\mathbf{x}_0)\cdot\mathbf{n}=0$ for $\mathbf{x}_0\in C$. This is a Fredholm integral equation of the first kind for Γ'. Here, we solve it numerically, following the approach taken for example in Nitsche and Krasny (1994): the sheet $\mathbf{x}(\alpha)$ is discretized by $n+1$ uniformly spaced points $\alpha_k, k=0,\ldots,n$. The no-through flow is imposed at the midpoints $\alpha_k^m=(\alpha_{k-1}+\alpha_k)/2$, $k=1,\ldots,n$, and the total circulation is prescribed. These $n+1$ conditions determine $\Gamma'(\alpha_k)$ for all k. The integrands are then known at all gridpoints and the second or fourth-order trapezoid approximation can be applied. We note that the second-order trapezoid rule is equivalent to the point vortex approximation of the sheet.

The required derivatives of $\mathbf{x}(\alpha)$ at α_p are determined from the initial distribution of points, $\mathbf{x}(\alpha)$, since the boundary C does not change in time. The required derivatives of $\Gamma'(\alpha)$ at α_p are computed using interpolation of values at the gridpoints obtained with second-order finite difference approximations. That is more than sufficient for the $O(h^2)$ method, but is necessary if an error reduction as $d\to 0$ is to be observed.

We present results for examples (a,c,d) in figure 8, each of which presents a different set of difficulties. The flat plate case (figure a) consists of a finite (nonperiodic) sheet with unbounded velocities near the two plate edges. An explicit expression for the potential flow is known and will be used for comparison. The two-cylinder problem (figure c) consists of two smooth periodic vortex sheets. Here, the main difficulty lies in solving for the sheet strength if the distance between the cylinders is small. The sheet strength on one cylinder, for example at the point $\mathbf{x}_0$ shown in the figure, depends on the velocity induced by the other cylinder, which is a near-singular integral if the cylinders are close. Inaccurate integration yields highly inaccurate sheet strength. This example is a simple planar version of the two-sphere problem considered in Siegel and Tornberg (2018). While an exact expression of the solution may be found, for example using the methods of Crowdy and Marshall (2005), our emphasis here is to determine the accuracy that can be attained numerically. Finally, example (d) presents the long term time evolution of separated flow past a plate, which is not possible to compute without accurately resolving the sheet motion near the boundary.

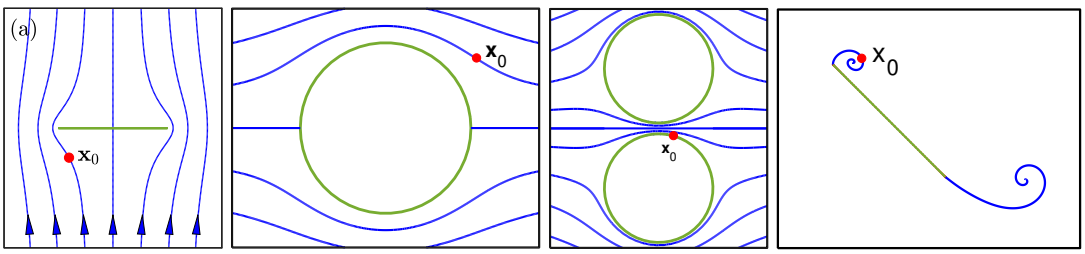

Figure 8. (a-c) Potential flow past plate and cylinders. (d) Vortex sheet separation at edges of plate inclined relative to a parallel background flow.

3.1. Potential flow past a flat plate.

The plate is positioned on the x-axis, on $x \in [-1,1]$, with upward far-field flow $\mathbf{U}_\infty = \langle 0, 1\rangle$. The plate is parametrized by $\mathbf{x}(\alpha) = \langle -\cos\alpha, 0\rangle, \alpha \in [0,\pi]$, and discretized uniformly in α,

$$\mathbf{x}(\alpha_k)\ , \quad \alpha_k = kh\ , \quad h = \pi/n\ , \quad k = 0,\ldots,n. \tag{18}$$

The resulting points are clustered near the edges, as shown in figure 9(a) for $n = 50$. Note that, as mentioned earlier, $\dot{\mathbf{x}} = 0$ at the tips $\alpha = 0, \pi$. In essence, the chosen point distribution amounts to using Chebbyshev points. However, the motivation is the form of the sheet strength $d\Gamma/dx$ near the tip, which, in proportion to the velocity magnitude, increases unboundedly as $1/\sqrt{1-x^2}$ as $x \to \pm 1$. With the given point distribution the scaled sheet strength $d\Gamma/d\alpha$ remains bounded at all points. Figure 9(b) shows the sheet strength at α_k computed as described above, for $n = 50, 100, 200, 400, 800$. The different curves are indistinguishable and differ from the exact solution $\Gamma'(\alpha_k) = -2\cos\alpha_k$ by $10^{-13} - 10^{-11}$, for all n, with increasing error as n increases due to increasing condition number. Thus the approach taken to obtain $\Gamma'(\alpha_k)$ gives sufficiently accurate results and is not responsible for the errors observed below.

3.1.1. Results of $O(h^2)$ corrected quadrature

Figure 9(a) also shows a red line crossing the plate vertically at a generic position that avoids the gridpoints. Figures 10(a,b) plot the horizontal and vertical velocity components u and v along this red line, vs y, obtained by evaluating (17a) using the uncorrected Trapezoid rule T_4 with $n = 50, 100, 200, 400, 800$. The exact velocity u is discontinuous and of opposite sign across $y = 0$, while $v \geq 0$ is continuous, symmetric across y, but decreasing to zero as the plate is approached. Figures (a,b) show that the Trapezoid rule recovers this behaviour away from the plate, but the errors near the plate are large. Figure (c) plots the absolute error, obtained by comparison with the known exact solution, vs the distance d from the plate. As n increases, the error is large in an interval of shrinking width, but the maximal error remains large for all n.

Figures (d,e) show the velocity using the $O(h^2)$ method described above, obtained by adding the corrections $E_4[\mathcal{H}_{11}]$, $\mathcal{H}_{11}$ as in (10c). Results are shown for all n, yet they are indistinguishable to the eye. The absolute error, plotted in figure (f), shows that the corrections reduce the errors in figure (c) by more than 10^4, already with $n = 50$. The maximum errors decreases by a factor close to 4 each time n is doubled, consistent with the assertion above that the method is $O(h^2)$. Figure (f) also shows that the error decreases as $d \to 0$, consistent with the assertion that the method is $O(hd, h^4)$. The bimodal shape of the error can be explained by the fact that, as shown later in §4, some of the errors $E[H_{jk}]$ are maximal when α_p is a gridpoint, while others are maximal when α_p is at distance d away from the gridpoints. The error plotted in figure (f) is dominated by a combination of $E[H_{jk}]$s with apparent bimodal shape. The error in the whole fluid domain is revisited below.

Figure 11(a) plots the flow streamlines computed by integrating (17b) with the Trapezoid rule, using $n = 50$ points on the plate. Figure 11(b) shows the result after adding the corrections $E_4[\mathcal{H}_{01}]$, where $\mathcal{H}_{01}$ is given in Table 1. The uncorrected results clearly show the local rotating fluid motion around the individual

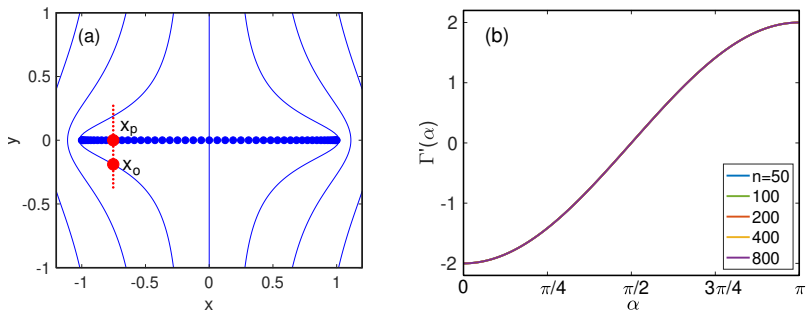

Figure 9. (a) Plate discretized by points, red line positioned at a generic x_0 between points, here $x_0 = -0.753$. (b) Circulation computed using $n = 50, 100, 200, 400, 800$ points, as indicated.

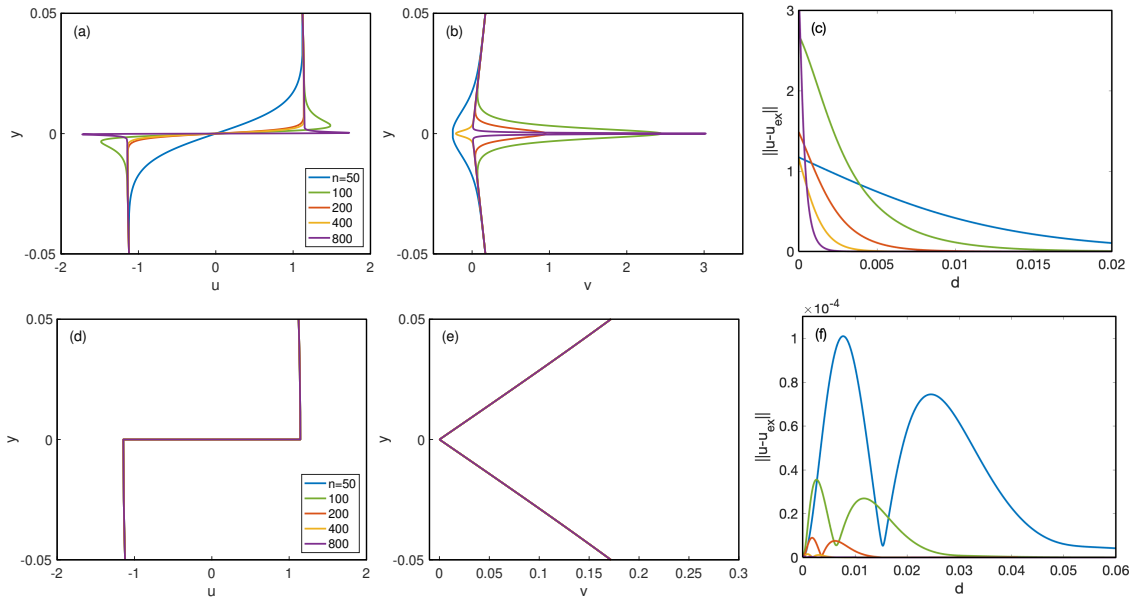

Figure 10. (a,b) Horizontal and vertical velocity along red line vs y, computed with Trapezoid rule T_4, (d,e) corrected velocity using the $O(h^2)$ quadrature, using $n = 50, 100, 200, 400, 800$ points, as indicated in (a). (c,f) Maximum errors vs d using T_4 and the corrected $O(h^2)$ quadrature.

vortices discretizing the plate. The correction reproduces parallel flow at the plate walls, consistent with the observation in figure 10(f) that the corrected error is highly accurate for small d.

While the inaccuracies of the Trapezoid approximation occur in a thin region near the plate, the effect on particle motion in the flow is significant. To illustrate, figures 12 and 13 present the evolution of a cloud of particles in the computed potential flow, using both the uncorrected velocity and the corrected $O(h^2)$ velocity, with $n = 50$ points on the plate. The particle position is evolved using the 4th-order Runge Kutta method. The particles are initially distributed in a circular region, with random phase, positioned at distance 0.5 below the plate. Figure 12 shows the computed position at a sequence of times $1.3 \leq t \leq 5$, where a small timestep $\Delta t = 10^{-5}$ was necessary in view of the unbounded velocities at the plate tips. Each frame shows the uncorrected results in the left column, and the corrected results in the right column. The initially circular cloud flattens as it approaches the plate. At time $t = 2.75$, oscillations are visible in the left column that are not present in the right. At times $t = 3.3, 3.9$, the particles in the left column are seen to cross the plate. This is consistent with the streamlines of the point vortex flow shown in figure 11(a). In the right

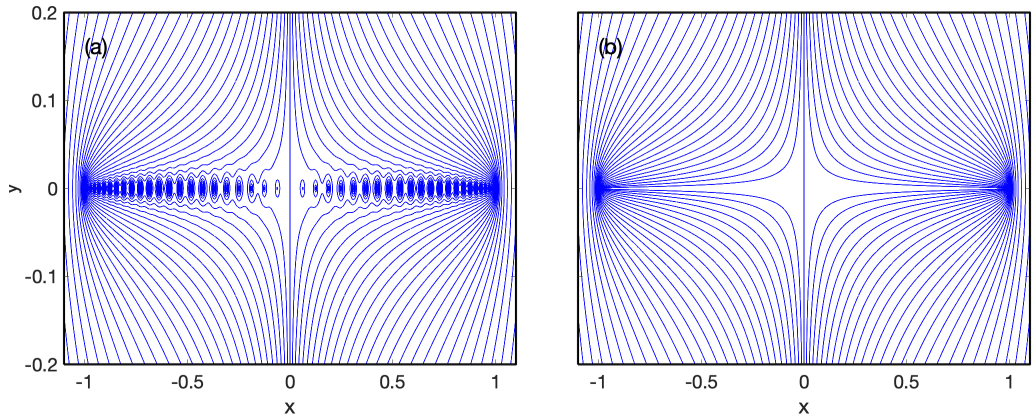

Figure 11. Streamlines computed with $n = 50$ and (a) trapezoid rule, (b) corrected $O(h^2)$ quadrature.

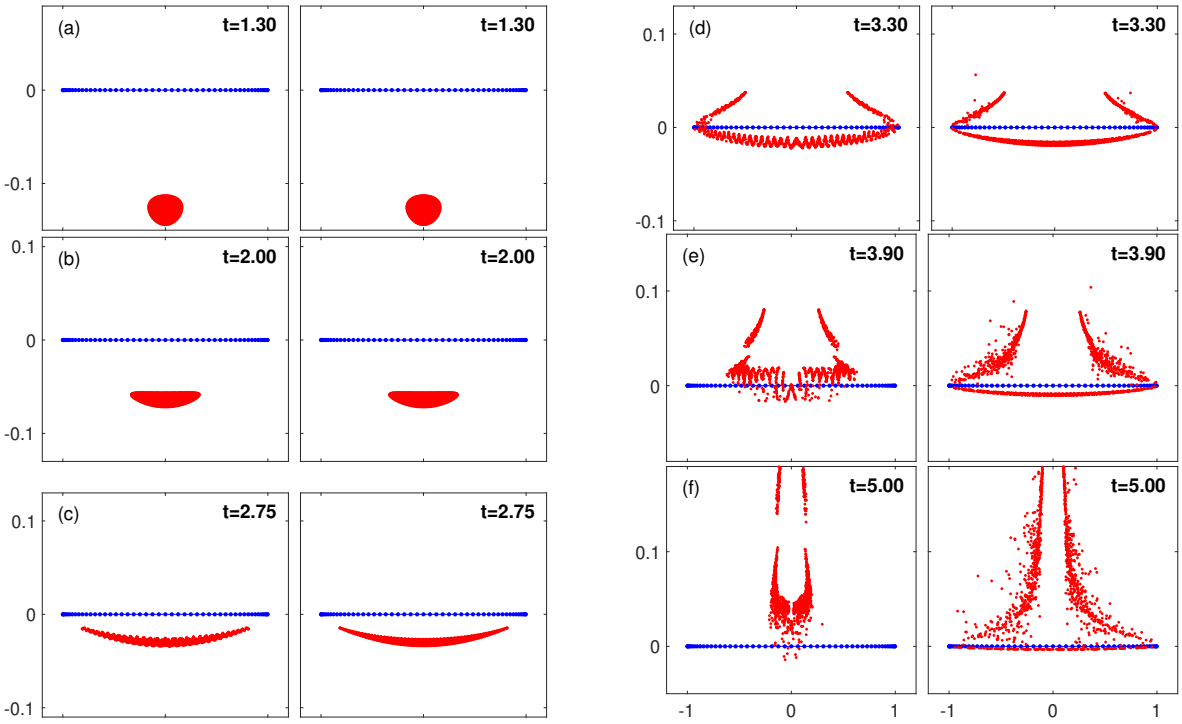

Figure 12. Position of cloud of points initially at distance 0.5 below the plate, at the indicated times. Each subplot shows results computed using the Trapezoid rule (left column), and the corrected $O(h^2)$ quadrature (right column), with $n = 50$.

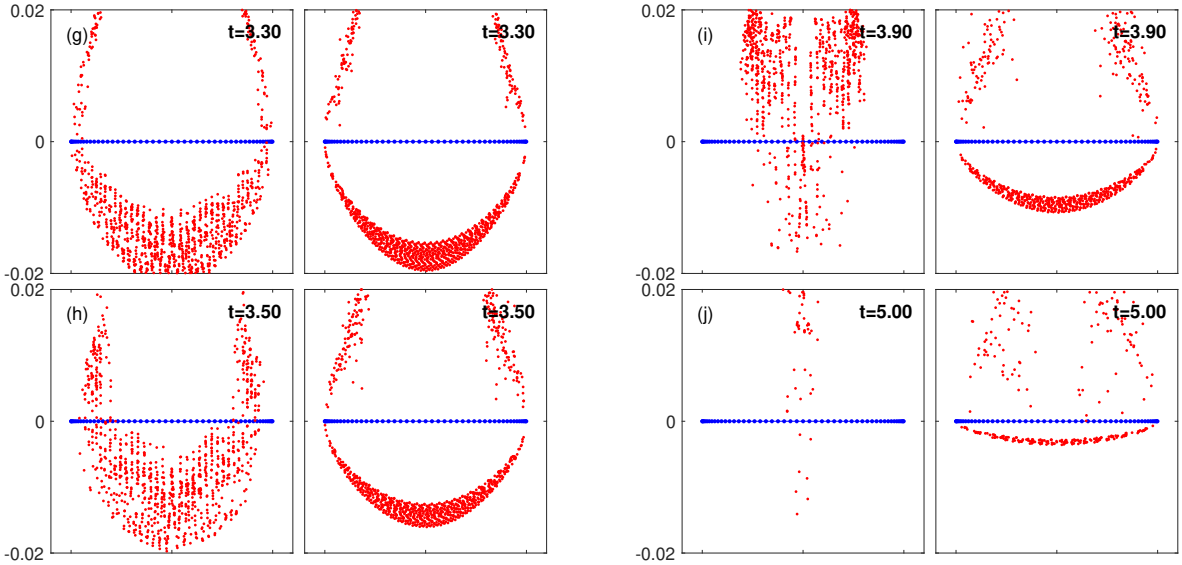

Figure 13. Closeup of solutions at the indicated times, computed using the Trapezoid rule (left column), and the corrected $O(h^2)$ quadrature (right column).

column of figure 12 showing the corrected results, the particles flow around the plate tips from bottom to top, with no apparent crossing through the plate.

Close inspection shows that indeed, with the corrected velocities none of the particles cross the plate. To illustrate, figure 13 shows a closeup of results for $3.3 \leq t \leq 5$. It clearly shows the uncorrected particle motion through the plate in the left column, and the corrected motion around the plate in the right column. Three movies showing the motion at three different scales are available for view as supplemental materials

of this paper. The closeup view in the third movie shows particles moving very close to the plate at late times $t = 8$-10, with none moving through it.

After the particles cross the plate, the corrected particle motion is asymmetric about the centerline. The reason for this is two-fold: the chosen initial particle distribution has random phase within a circular region and is thus not left-right symmetric. However, in addition, the errors near the plate tips, where the fluid velocity is unbounded, are large. As shown later in figure 15, the maximal relative error using the $O(h^2)$ method with $N = 50$ is 4%. Such errors are sufficient to break any initial symmetry in the point position after they pass by the plate tips. The main point in figures 12-13 is to show precisely that with few points, such as $N = 50$, the through-plate-problem is resolved.

3.1.2. Observed rate of convergence, $O(h^2)$ and $O(h^3)$ methods.

Figure 10 above shows the error in the computed velocity along a line. Figure 14 shows the relative error $||\mathbf{u} - \mathbf{u}_{ex}||_2/||\mathbf{u}_{ex}||_2$ on a fine rectangular grid around the whole plate. The left column (figures a,d) shows results using the uncorrected Trapezoid method, the middle column (figures b,e) shows results using the corrected $O(h^2)$ method, and the right column (figures c,f) shows results using the corrected $O(h^3)$ method. The top row is computed with $n = 50$, the bottom with $n = 800$. Here, $\mathbf{u}$ and $\mathbf{u}_{ex}$ are the computed and the exact velocity at a gridpoint $\mathbf{x}$ and the norm used is the Euclidean 2-norm.

The errors in the point vortex approximation in figures (a,d) diverge to infinity as the vortices are aproached, when both d and $ah \to 0$. The gridpoints chosen in the figures avoid the plate, and are positioned at distance $d \geq 0.0005h$ for both $n = 50$ and $n = 800$. Thus the maximal errors of the Trapezoid approximation are large but bounded on the grid. The errors are shown on a logarithmic color scale from 10^{-12} to 10^2, with all errors $< 10^{-12}$ shown as dark blue, and all errors $> 10^2$ shown as bright yellow. Figure (a) clearly shows the large errors near each of the point vortices. The errors decrease as the distance to the plate increases. The errors are approximately constant along elliptical level curves. In view of the chosen point distribution, the set of points $\mathbf{x}$ whose distance to the plate is a constant multiple of the distance $\Delta s(\mathbf{x})$ between the

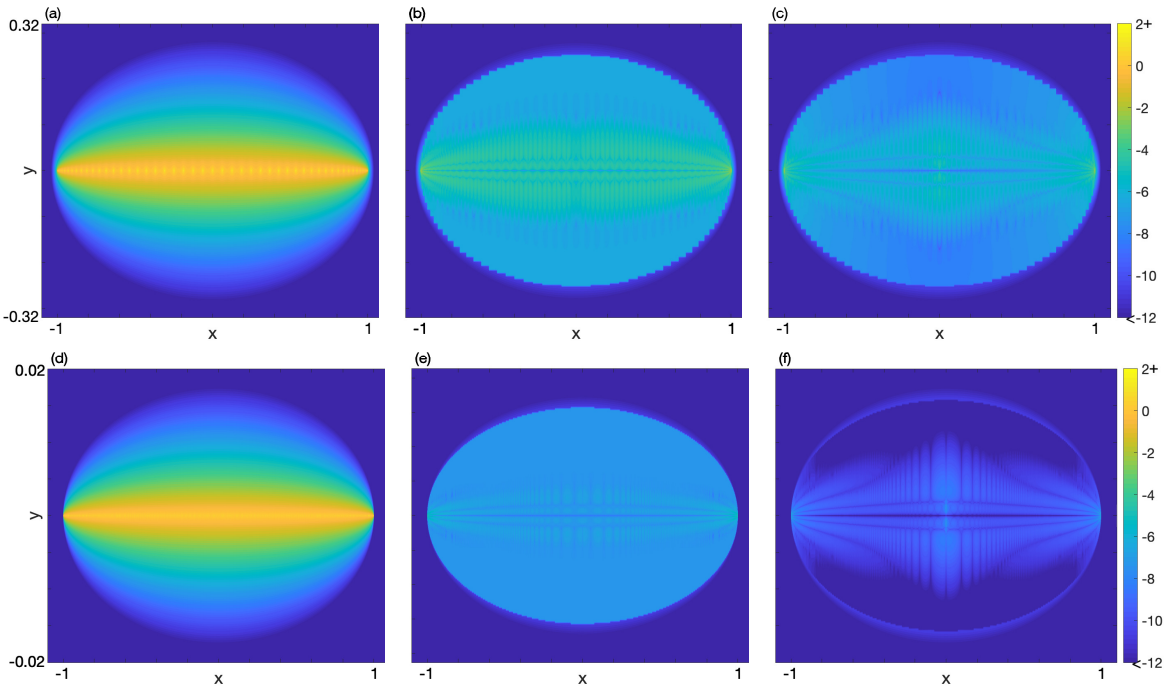

Figure 14. Relative error $||\mathbf{u} - \mathbf{u}_{ex}||_2/||\mathbf{u}_{ex}||_2$ on a fine grid, computed with (a,d) Trapezoid rule, (b,e) $O(h^2)$ quadrature, (c,f) $O(h^3)$ quadrature. The top row (a,b,c) shows results for $n = 50$, the bottom row (d,e,f) for $n = 800$. The errors are plotted using a logarithmic color scale, where all errors bigger than 10^2 and less than 10^{-12} are incorporated in the top yellow and bottom blue colors.

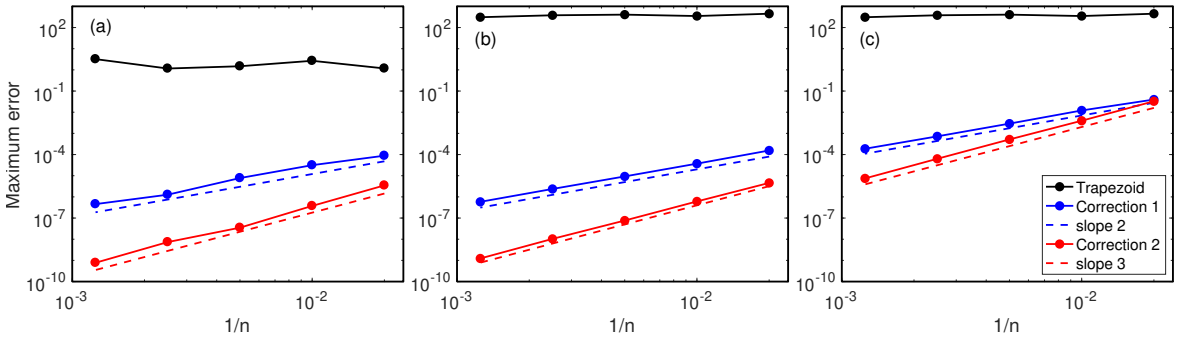

Figure 15. Maximal errors over all points on a grid over (a) the line $x = -0.753$, (b) region away from tip, $|x| \leq 0.8$, (c) the whole domain shown. Errors for $n = 50$, 100, 200, 400, 800 meshpoints are shown. The error that is maximized is the minimum of the relative error and the absolute error.

two nearest gridpoints on the plate, forms an ellipse. Thus the error is proportional to $\Delta s(\mathbf{x})$. Consistent with these remarks, note that the vertical scale for $n = 800$ is a factor of 16 smaller than the vertical scale for $n = 50$, that is, proportional to $\Delta s(\mathbf{x})$.

The correction is applied to points $\mathbf{x}$ that are within $4\Delta s(\mathbf{x})$. Per the previous discussion, this represents an elliptical region around the plate. All corrected error plots (b,c,e,f) clearly show the elliptical region in which the correction has been applied. Near the plate the corrected errors are small, as shown by the dark blue center line. At moderate distances the errors have a bimodal shape with increasing d, as seen earlier in figure 10(f). At large distances, $d \approx 4\Delta s$, the errors in the $O(h^2)$ results in (b,e) are larger than the uncorrected results outside the ellipse. On the other hand, the $O(h^3)$ results with $n = 800$ shown in figure (f) in the ellipse are as accurate as the uncorrected results outside of the ellipse. Finally, note that the relative error near the plate edges is somewhat larger than away from the edges. The relative error near the origin is also larger, as visible specially in (f), since the actual velocities there are small.

The maximal errors

$$\max_{\mathbf{x}\in D}\left[\min\left(\frac{||\mathbf{u}-\mathbf{u}_{ex}||_2}{||\mathbf{u}_{ex}||_2}, ||\mathbf{u}-\mathbf{u}_{ex}||_2\right)\right] \tag{19}$$

for the three methods shown in figure 14 are plotted in figure 15, versus $1/n = h/\pi$. The maximum of the smaller of the absolute and the relative error is plotted to avoid large relative errors when the velocity is small. Figures 15(a,b,c) plot the maximal errors over different regions D using the uncorrected Trapezoid method (black), the $O(h^2)$ method (blue) and the $O(h^3)$ method (red). Figure (a) plots the maximal errors along the line considered in figure 10. The uncorrected errors are large, do not decay as n increases, and are irregular since the relative distance ah to the nearest point vortex changes irregularly as n increases. The corrected values are 5 to 10 orders of magnitude smaller. Figure (b) plots the maximal errors in the region $|x| < 0.8$ away from the plate edges. The values are similar to (a). Figure (c) plots the maximal errors everywhere and captures the larger relative errors near the plate edges. Throughout, the results with the $O(h^2)$ and the $O(h^3)$ methods clearly decay as predicted.

3.1.3. Effects of finite precision as $d \to 0$.

The above results show that in this sample application the asserted convergence rates hold, and in theory, arbitrarily high accuracy can be obtained as $h \to 0$. However, if $d \ll 1$, the effects of finite machine precision are larger than one may expect. The method consists of adding a correction to a bad result. In case of the point vortex approximation, the errors are unbounded as $d \to 0$. Thus, the bad error can be arbitrarily large, depending on the closeness of the target point to the point vortices. A correction that is accurate to 14 digits can only gain 14 digits of accuracy, which may not be enough to obtain small errors. Phrased differently, the problem if $d \ll 1$ is given by loss of significance due to subtraction of two large numbers $T_4[G]$ and $E_4[\mathcal{H}]$ in equation (6). This problem is the same in either formulation (6b) or (6c). For the results shown in figures 14 and 15, we observed this situation for $d = 0.0005h$ (the closest gridpoints). In that case the uncorrected point vortex error can be estimated to be ≈ 300. For the $O(h^3)$ correction to correctly reduce

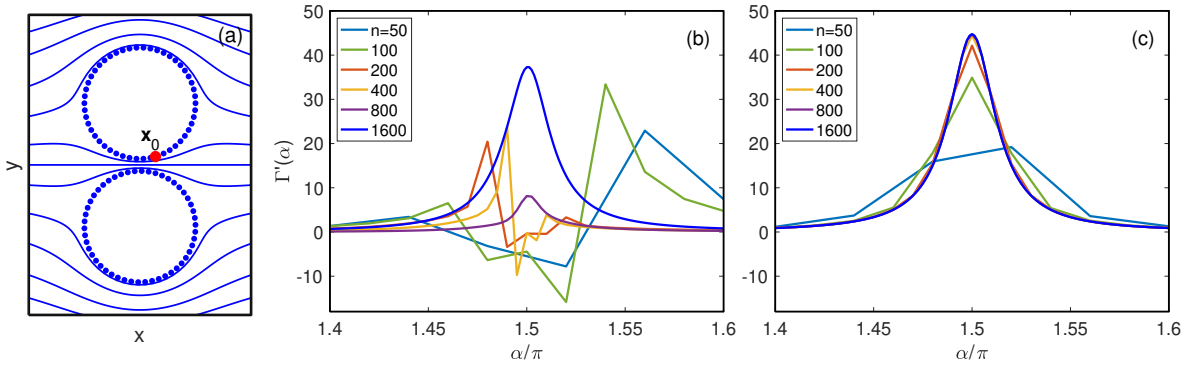

Figure 16. Flow past two cylinders of radius $R = 1$ separated by distance $2A$. (a) Sketch showing discretization of boundary, nonsymmetric with $\alpha_{off} = h/4$. (b,c) Computed circulation distribution $\Gamma'(\alpha)$ along the top cylinder, for $A = 0.001$ and $\alpha_{off} = h/4$, using the indicated values of n, with (b) Trapezoid rule, (c) corrected $O(h^3)$ quadrature.

the error to 10^{-10} the addition was performed in quadruple machine precision. A simple solution consists of noting that the extremely small distances where this problem occurs can be estimated, and within those regions, simple linear interpolation works well. For example, obtaining 5 digits of accuracy is difficult if $d < 10^{-8}h$. For those distances linear interpolation between $d = 0$, where the integral can be evaluated accurately, and $d = 2 \cdot 10^{-8}h$ typically would yield 5 or more digits of accuracy.

3.2. Potential flow past two cylinders.

Our second example consists of potential flow past two cylinders. The cylinders have radius 1, are separated by a distance A, centered at $(0, 1 \pm A/2)$, in a far-field background flow $\mathbf{U}_\infty = \langle 1, 0\rangle$. The two bounding vortex sheets are parametrized by $\mathbf{x}_\pm(\alpha) = \langle \cos\alpha, \sin\alpha \pm (1 + A/2)\rangle$, $\alpha \in [0, 2\pi]$ and discretized by equally spaced points

$$\mathbf{x}_+(\alpha_k)\ , \quad \mathbf{x}_-(\alpha_k + \Delta\alpha)\ , \quad \alpha_k = kh\ , \quad h = 2\pi/n\ , \quad k = 0, \ldots, n \tag{20}$$

Here, $\Delta\alpha \neq 0$ adds a small rotation to the points on the bottom cylinder. Generically, the discretization of nearby objects is not necessarily symmetric. In the present example, perfect symmetry $\Delta\alpha = 0$ was found to improve the results significantly. This was also observed by Elling (2020), who, for this reason, uses symmetric points to perform symmetric vortex sheet calculations. Here we consider generic nonsymmetric distributions and use a representative value $\Delta\alpha = h/4$. Figure 16(a) shows the resulting nonsymmetric point vortex positions for $n = 50$.

Figure 16(b,c) shows the computed sheet strength along the top cylinder for $A = 0.002$. It shows a closeup of $\Gamma'(\alpha_k)$ near $\alpha = 1.5\pi$, which is the point on the top cylinder closest to the bottom cylinder. The sheet strength at a point $\mathbf{x}_0$ on the top cylinder depends on the velocity induced by the bottom cylinder. In figure (b) this velocity is computed by the uncorrected Trapezoid rule. If $\mathbf{x}_0$ is near the bottom cylinder, the resulting inaccuracies lead to large errors in the resulting sheet strength, with no convergence apparent for all $n \leq 1600$ shown. Figure (c) shows the results obtained when the induced velocity is computed using the corrected quadrature. Clear convergence is observed, with the $n = 100$ results about as good as the $n = 1600$ results in figure (b). These results are computed with the $O(h^3)$ method, although they are, to the eye, indistinguishable from the $O(h^2)$ results (not shown). The sheet strength shown in (c) converges fast. For example, the error in the maximum value at $\alpha = 1.5\pi$, starting with $n = 100$, decreases by factors 3.8, 10.3, 32.0 every time n is doubled. The value at $\alpha = 1.52\pi$ starting with $n = 50$, decreases by factors 1.5, 8.0, 64.3, 111.3, every time n is doubled.

Figure 17 plots streamlines for the flow past two cylinders separated by $A = 0.02$, where both sheet strength and streamlines are computed with $n = 50$ and (a) the Trapezoid rule, (b) the corrected $O(h^3)$ quadrature. The result in (a) shows lack of symmetry about both $x = 0$ and $y = 0$, and many streamlines traversing the cylinders. The result in (b) recovers all expected symmetries and has no streamlines crossing the boundary. Only a small irregularity is seen near the origin. This irregularity is slightly more noticeable with the $O(h^2)$ method (not shown). Figure 18 (a,b) shows a closeup of the streamlines shown in figure 17

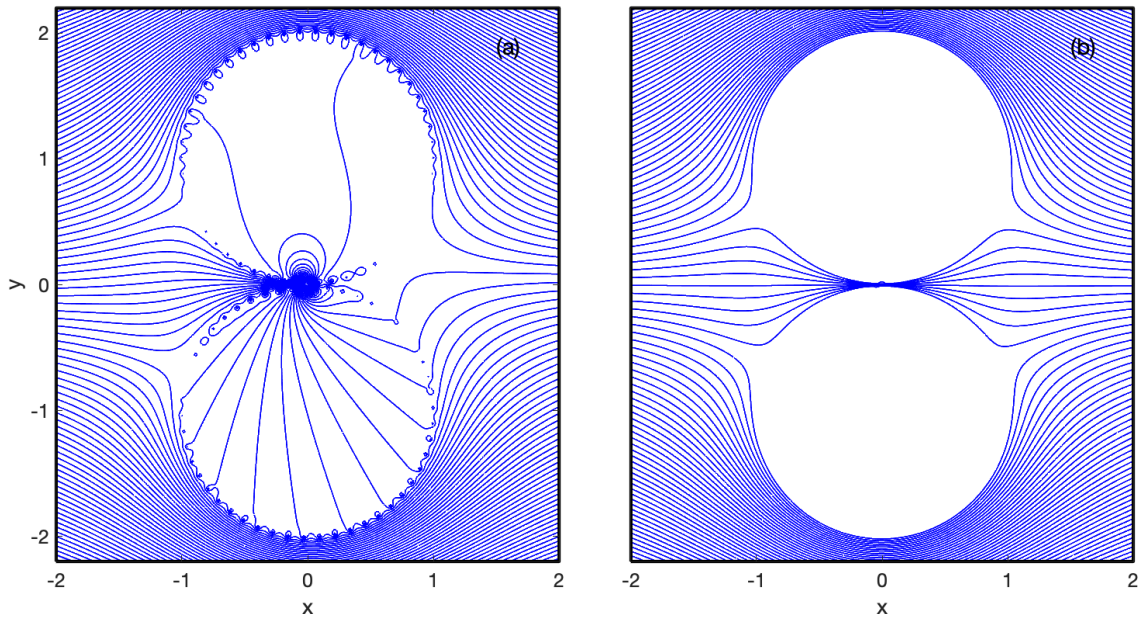

Figure 17. Potential flow past two cylinders of radius 1, separated by half-distance $A = 0.01$, computed with $n = 50$ points on each cylinder, using (a) the trapezoid rule and (b) the corrected $O(h^3)$ quadrature.

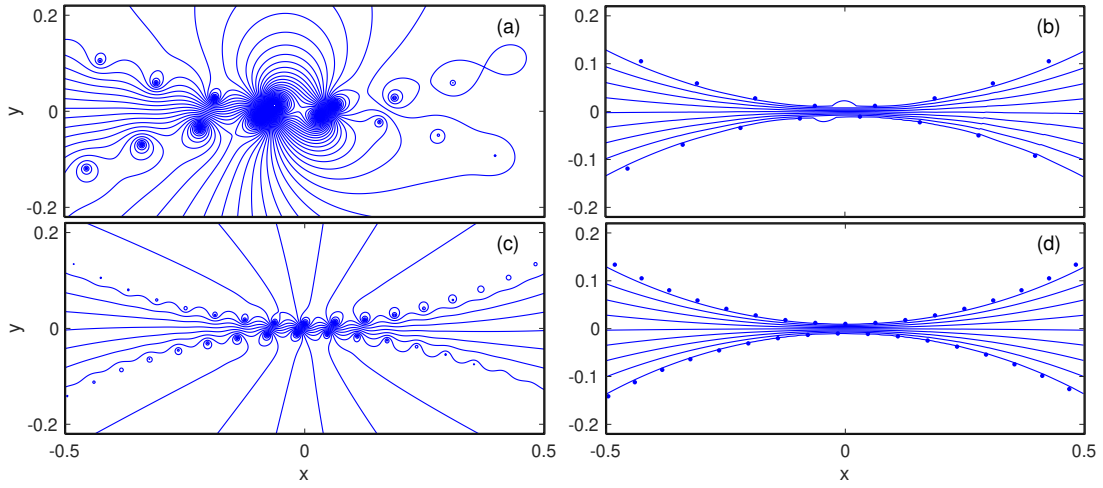

Figure 18. (a,b) Closeup of figure 17, using $n = 50$. (c,d) Same as (a,b), but using $n = 100$.

near the origin, and more clearly shows the shape of the irregularity in (b) in the streamlines closest to the boundary. As reference, the $n = 50$ gridpoints are indicated. The size of the gap between the cylinders is about 1/6 the distance between gridpoints. Figure 18 (c,d) shows the streamlines computed with $n = 100$, showing that the irregularity in figure (b) is resolved.

These results show that the corrected quadrature, by accurately recovering the velocity induced by the nearby cylinder, yields accurate sheet strength and streamlines.

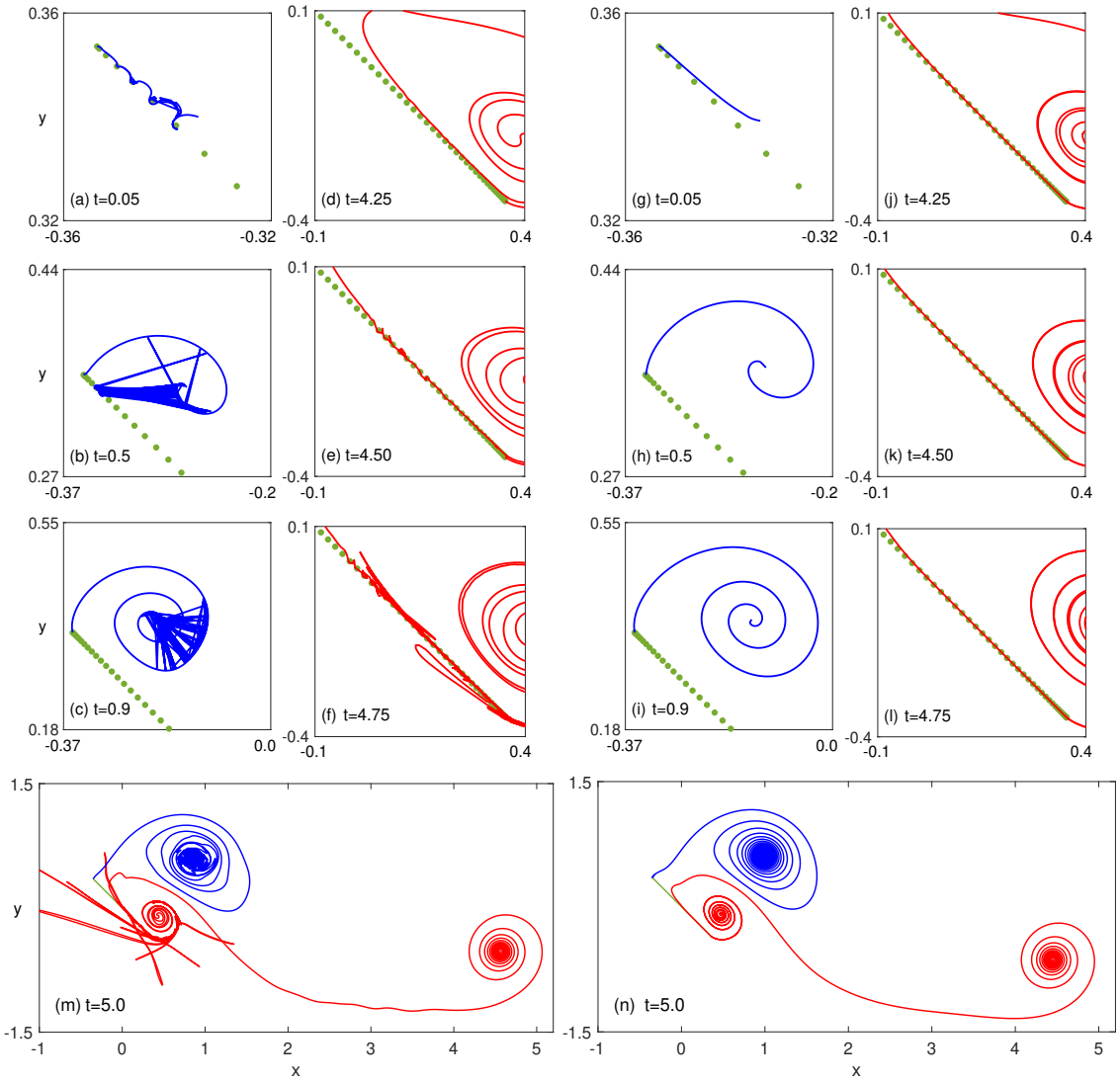

Figure 19. Vortex sheet separation at the edges of an inclined plate in a parallel background flow, at the indicated times. The plate is discretized by points shown in green. The vortex sheet separated from the right plate tip is shown in red, the one separating from the left is shown in blue. Figures (a-f,m) on the left are computed using the uncorrected trapezoid rule (point vortex approximation). Figures (g-l,n) on the right are computed using the corrected $O(h^3)$ quadrature.

3.3. Vortex sheet separation past plate

The last example regards the simulation of inviscid vortex sheet separation at the edges of a plate inclined at 45 degrees relative to an incoming parallel flow, as illustrated in figure 8(d). The parallel far-field velocity is $\mathbf{U}_\infty = \langle 1, 0\rangle$. The plate is centered at the origin and has length 1. The vortex separation is computed using a well-established method, following Nitsche and Krasny (1994); Nitsche (1996); Sheng *et al.* (2012); Huan, Nitsche and Kanso (2015, 2016); Xu, Nitsche and Krasny (2017). The plate is discretized by point vortices, similar to the plate in §3.1. At each timestep, vorticity is shed from the edges so as to satisfy the Kutta condition, forming a vortex sheet that rolls up under its self-induced velocity. Similar vortex sheet separation models have been proposed and used by several researchers, eg see Jones (2003); Jones and Shelley (2005); Alben (2015); Sohn (2020); Shukla and Eldredge (2007); Darakananda *et al.* (2018).

The near-singular problem occurs when points on the separated sheet approach the plate. The left side of figure 19 (figures a-f,m) show the difficulties that can occur at different times during the flow. Figures (a-c) show a closeup of the separation at the left plate edge near $t = 0$. Shed vortices are initially close to

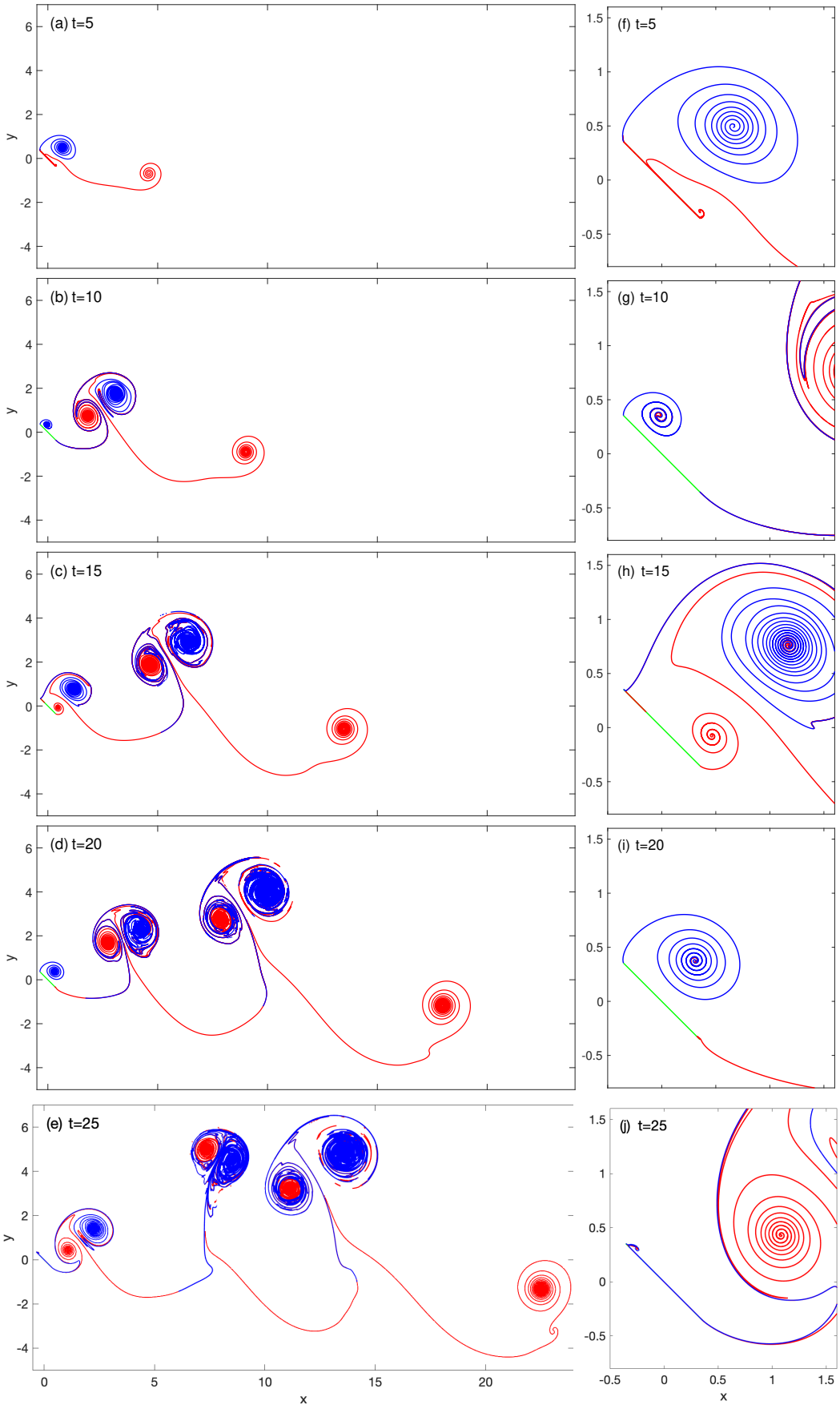

Figure 20. Vortex sheet separation at edges of an inclined plate, at times $0 \leq t \leq 25$. The fluid velocity is computed using the corrected $O(h^3)$ quadrature. Figures (f-j) show closeups of figures (a-e).

the plate (figure a) and without any other type of control they will get entangled by the individual point vortices discretizing the plate, as we observed earlier, for example in figures 11 and 12. Once the shed vorticity is sufficiently strong the sheet may move sufficiently far from the plate, as in figures (b,c), but it stays entangled due to the earlier irregular point motion. Figures (d-f) show a closeup of the separation at a later time near the right vortex. Here an outer vortex turn approaches the inviscid slip plate wall and again is entagled by the plate once it gets too close. As a result, the motion becomes highly irregular and the simulation soon breaks down. This particular simulation breaks down shortly after $t = 5$ shown in figure (m). We note that throughout, blue denotes vorticity separated from the left plate edge and red denotes vorticity separated from the right plate edge.

Figures 19(g-l,n), on the right side, show simulation results using the same timestepping and plate discretization parameters as the left side but computing the velocity with the corrected $O(h^3)$ method instead of the trapezoid rule. The timestep in both simulations increases from $\Delta t = 0.0001$ initially to $\Delta t = 0.002$ at $t = 1$, after which it remains constant, and there are $n = 64$ points on the plate. The figures show that with the correction there is absolutely no entanglement and the simulation proceeds cleanly for a long time. Note that also the small wiggles observed at time $t = 5$ in figure (m) between the first rightmost red vortex and the next red vortex have also dissapeared in (n). This shows that accurate smooth vortex motion near the plate leads to smooth circulation shedding.

Figure 20 shows results using the $O(h^3)$ method for long times $0 \le t \le 25$. Figures (a-e) show the flow at a large scale at the indicated times, while figures (f-j) show closeups near the plate at the same times. There is repeated vortex shedding from both plate edges. The shed vorticity from the right is positive (red), while the one from the left is negative (blue). This results in a vortex pair being shed at regular time intervals. At time $t = 25$ there are three well-formed vortex pairs in the flow, plus the initial red vortex furthest up front, and the beginning of the formation of a blue vortex at $t = 25$. The figure shows that no irregular motion or entanglement occurs even though the sheet repeatedly approaches the plate extremely closely, as shown in the closeups on the right. In principle further vortex shedding can be computed without numerical difficulties. The only limit to this calculation is the total computing time. At $t = 25$ there are about $180,000$ point vortices in the flow. The total runtime was 4.1 days on a single processor of a desktop computer.

Indeed, at all times after the second right vortex shedding ($t \approx 3.3$) does a portion of the separated sheet lie arbitrarily close to the plate. This is more clearly visible in the movies available for view as supplemental materials of this paper. The movies show the vortex sheeet separation over $0 \le t \le 25$, computed with the $O(h^3)$ method, at three different scales. They show that the corrected velocity accurately resolves the motion near the plate, without which the long term simulation would not be possible. Thus, the proposed method accurately and effectively resolves the near-singular velocities in this complex flow.

4. Convergence of $E_4[H_{jk}]$

The previous section showed that the method proposed here is effective in computing near-singular integrals accurately, and that the convergence rates derived in §2.4 are achieved in practice. The only step that remains is to prove equations (12ab) required for the argument in §2.4. That is,

$$E_4[H_{jk}] = O(hd^{k-2j}) \ , \tag{21a}$$

$$E_4[H_{0k}] = \begin{cases} O(h\log d) \ , & \text{if } k = 0, \\ O(h^{k+1}) \ , & \text{if } k > 0, \end{cases} \tag{21b}$$

in addition to an $O(h^4)$ or an $O(h^4 \log h)$ term if $k \ge 2j + 4$, where

$$H_{jk} = \frac{\hat{\alpha}^k}{(d^2 + c^2\hat{\alpha}^2)^j}, \quad j \ge 1, k \ge 0 \ , \tag{22a}$$

$$H_{0k} = \hat{\alpha}^k \log(d^2 + c^2\hat{\alpha}^2), \, k \ge 0 \ , \tag{22b}$$

and $\hat{\alpha} = \alpha - \alpha_p$. We note that c^2 is always bounded away from 0 when d is sufficiently small, as argued earlier (see also Appendix A), and thus it is sufficient to consider $c^2 = 1$ for the arguments below. We

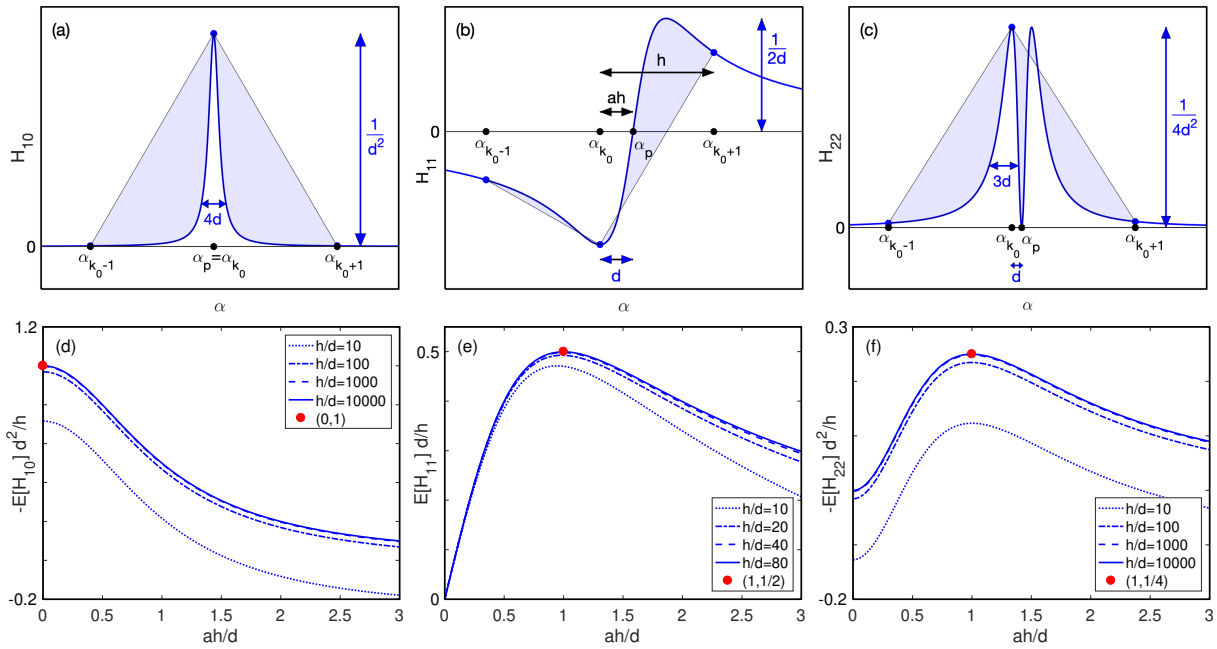

Figure 21. Error $E[f]$ over $I = [(k_0 - 1)h, (k_0 + 1)h]$, for (a,b) f_1, (c,d) f_2, (e,f) f_3. The left column shows the error, represented by the shaded area, for sample values of a, d, h. The right column plots scaled values of $E[f]$ for a range of a, d, h.

first address the proper fractions H_{jk}, $j \geq 1$, with $k < 2j$, then generalize the result to improper fractions $k \geq 2j$, and lastly consider the logarithmic functions H_{0k}.

4.1. Proper fractions H_{jk}, $j \geq 1$, $k < 2j$

Here we consider proper fractions $H = H_{jk}$ where $j \geq 1$ and $k < 2j$, with $c = 1$. Our goal is to bound $E_4[H] = \int_I H - T_4[H]$. To begin, note that it is sufficient to consider a small interval $I = [\alpha_{k_0-1}, \alpha_{k_0+1}]$ consisting of three gridpoints, where α_{k_0} is the point closest to α_p. As shown below, the near-singular behaviour of H occurs in an interval of width $O(d)$ centered at α_p. Therefore, for small d/h, the interval I of size $2h$ around α_p captures the leading order contribution to $E_4[H]$ over any larger interval. Similarly, the endpoint contributions which make up the difference between $T_4[H]$ and the standard trapezoid rule $T[H]$ are relatively small, thus

$$E_4[H] \approx E[H] = \int_I H - T$$

where

$$T = T[H] = \frac{h}{2}[H(\alpha_{k_0-1}) + 2H(\alpha_{k_0}) + H(\alpha_{k_0+1})] \ . \tag{23}$$

The approach to bound $E[H]$ becomes clear by considering some examples. The three sample functions H_{10}, H_{11}, H_{22} are plotted in figure 21(a,b,c) for generic values of d. Their maximum values and characteristic lengthscales are indicated. Like all functions H_{jk}, they have a self-similar shape

$$H_{jk} = \frac{\hat{\alpha}^k}{(d^2 + \hat{\alpha}^2)^j} = \frac{1}{d^{2j-k}} \frac{u^k}{(1+u^2)^j} = \frac{1}{d^{2j-k}} g_{jk}(u) \tag{24}$$

where $u = \hat{\alpha}/d$. For $k < 2j$, $g_{jk}(u)$ is a bounded function that vanishes as $u \to \pm\infty$. As a result, the maximum value of $|H|$ satisfies

$$|H_{jk}|_{max} = \frac{|g_{jk}|_{max}}{d^{2j-k}} = O(d^{k-2j}) \ , \tag{25}$$

Also, characteristic widths of the near-singular behaviour are $O(d)$. For example in figure (a), $4d$ is the width of the interval where $H_{10} \geq |H_{10}|_{max}/5$. In figure (c), $3d$ is the width of the interval defined by $H_{22} = 4|H_{22}|_{max}/13$. In figure (b), d is the half-distance between the points at which H_{11} is extremal.

Figures 21(a,b,c) also show the three gridpoints $\alpha_{k_0-1}, \alpha_{k_0}, \alpha_{k_0+1}$, equally spaced by distance h. The shaded area represents the trapezoid error $E[H] = \int H - T$ over the chosen interval $I = [\alpha_{k_0-1}, \alpha_{k_0+1}]$. As we saw earlier, the error depends not only on the meshsize h and the distance d, but on the distance ah from α_p to the closest gridpoint α_{k_0} (see figure 21b). Here $a \in [-1/2, 1/2)$, where positive a corresponds to $\alpha_p > k_0 h$, and negative a corresponds to $\alpha_p < k_0 h$. We need to bound $E[H]$ over all values of ah. By symmetry of all basis functions H_{jk} it is enough to consider $a > 0$.

In all three figures 21(a,b,c) the value of $ah \geq 0$ is chosen so that the maximum of $|H|$ is taken on at the middle gridpoint α_{k_0}. This choice of ah is crucial for our argument. The key point is to recognize that if $d \ll h$, then:

(1) The trapezoid approximation T is largest in magnitude when ah is such that the maximum of $|H|$ is taken on at the middle gridpoint, α_{k_0}. In that case, the value of T, given in (23), is dominated by the contribution of the middle gridpoint, $h|H(\alpha_{k_0})| = h|H|_{max}$. That is,

$$|T|_{max} \approx h|H|_{max} \ , \tag{26a}$$

where $|T|_{max} = \max_{a \in [-1/2, 1/2)} |T|$.

(2) The maximal trapezoid approximation is much larger in magnitude than the integral of H

$$|T|_{max} \gg \left| \int_I H \right| \ . \tag{26b}$$

Since $|E[H]| = |\int H - T| \leq |\int H| + |T| \leq \int |H| + |T|_{max}$, it follows from (26b) that $|T|_{max}$ *is the dominant contribution to the error* $E[H]$. It then follows from (26a) that

$$|E[H]|_{max} \approx |T|_{max} \approx h|H|_{max} \ , \tag{27}$$

and that this maximum is taken on when ah is such that $|H|$ is maximal at α_{k_0}. Finally, using the scaling (25) for H_{max} we obtain the desired bound:

$$E[H_{jk}] = O(hd^{k-2j}) \ . \tag{28}$$

Item (1) follows from equation (23) and the self-similar nature of H: the middle term in (23) is largest when H is maximized at α_{k_0}, and the relative values of H/H_{max} at any other grid point α_k vanish as $d \to 0$. Item (2) can be deduced from the figures: for example, if H is even, as in figures 21(a,c), $|T|_{max}$ approximately equals the area of the triangular region under the two slanted lines, which is clearly bigger than the area of the white region under the curve $y = H(\alpha)$ for small d/h. If H is odd, as in figure 21(b), then $\int H \approx 0$ by symmetry, and $|T| \approx h|H|_{max} \gg 0$.

To illustrate these results, figures 21(d,e,f) plot the actual errors $E[H]$ for the three sample functions H_{10}, H_{11}, H_{22}, scaled by the predicted behaviour (28), as functions of ah/d, for a range of values of a, d, h. The red dots represent the predicted approximate maximum values of $E[H]$ and the value of ah/d at which it ocurrs. For example, for $H_{10}(\alpha)$, shown in figure 21(a), the maximum is $1/d^2$ and taken on at $\hat{\alpha} = 0$. Thus $|E[H_{10}d^2/h|_{max} \approx 1$, taken on when $ah/d = 0$. For $H_{11}(\alpha)$, shown in figure 21(b), the maximum is $1/2d$, taken on at $\hat{\alpha} = d$. Thus $|E[H_{11}d/h|_{max} \approx 1/2$, taken on when $ah/d = 1$. The figures show that as $h/d \to \infty$, the actual error, scaled appropriately, quickly converges to a limiting curve with magnitude closely bounded by the ordinate of the red dot. These results illustrate the accuracy of the approximation (27) and are consistent with the main conclusion (28). We remark that the curves shown in figures (b,d,f) capture the scaling and the dependence of the error on all three parameters h, d and a.

4.2. Nonproper fractions H_{jk}, $j \geq 1$, $k \geq 2j$

The result for non-proper fractions is obtained from the above result (28), now switching from T to T_4, using long division and the fact that polynomials of degree $p \leq 3$ are integrated exactly by the trapezoid

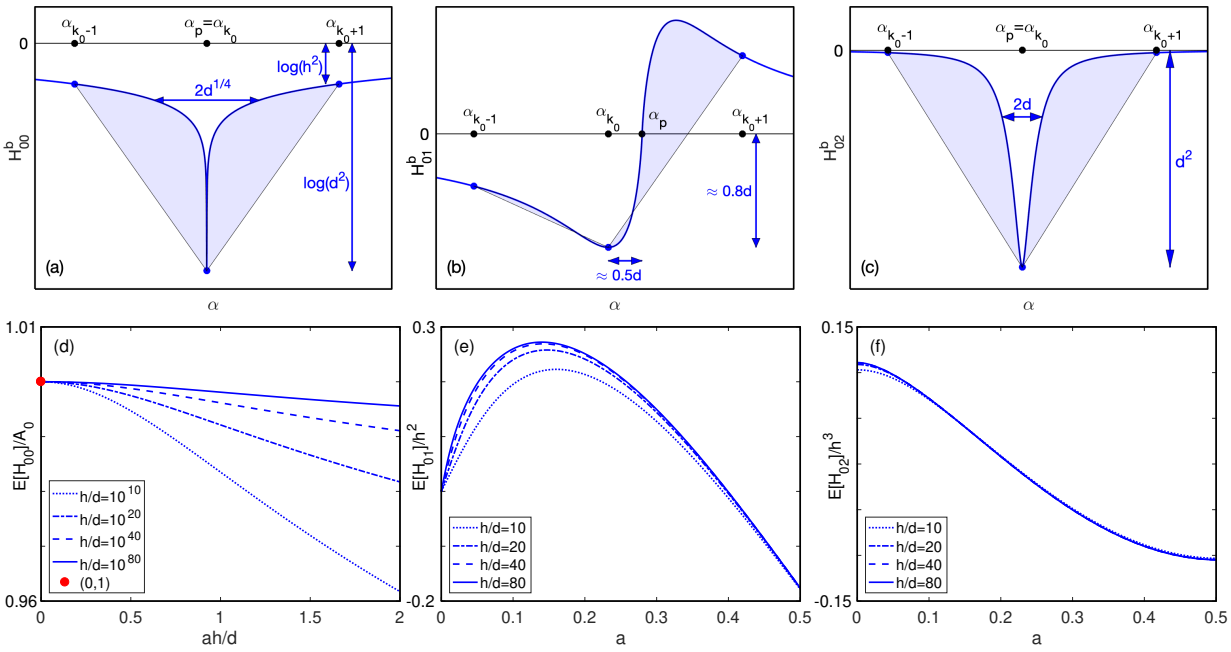

Figure 22. (a,b,c) Graphs of the bounded components H^b_{0k} for $k = 0, 1, 2$, for generic values of h, d. The value of a is chosen to maximize the trapezoid error, which is represented by the shaded area. Characteristic length scales are indicated. (d,e,f) Scaled errors $E[H_{0k}]$, $k = 0, 1, 2$, for a range of values of a, h, d. In (d), $A_0 = 2h(\log(d/h) + 2) + 2d\pi$ approximates the shaded area in (a).

rule T_4. For example,

$$H_{12}(\alpha) = \frac{\hat\alpha^2}{d^2+\hat\alpha^2} = 1 - d^2\frac{1}{d^2+\hat\alpha^2}, \quad \Rightarrow \quad E[H_{12}] = O(h)\ , \tag{29a}$$

$$H_{13}(\alpha) = \frac{\hat\alpha^3}{d^2+\hat\alpha^2} = \hat\alpha - d^2\frac{\hat\alpha}{d^2+\hat\alpha^2}, \quad \Rightarrow \quad E[H_{13}] = O(hd)\ , \tag{29b}$$

$$H_{24}(\alpha) = \frac{\hat\alpha^4}{(d^2+\hat\alpha^2)^2} = \frac{\hat\alpha^2}{d^2+\hat\alpha^2} - d^2\frac{\hat\alpha^2}{(d^2+\hat\alpha^2)^2}, \quad \Rightarrow \quad E[H_{24}] = O(h)\ , \tag{29c}$$

$$H_{25}(\alpha) = \frac{\hat\alpha^5}{(d^2+\hat\alpha^2)^2} = \frac{\hat\alpha^3}{d^2+\hat\alpha^2} - d^2\frac{\hat\alpha^3}{(d^2+\hat\alpha^2)^2}, \quad \Rightarrow \quad E[H_{25}] = O(hd)\ . \tag{29d}$$

These results can be generalized using induction to obtain that for all $k \geq 0$,

$$E_4\left[\frac{\hat\alpha^k}{(d^2+\hat\alpha^2)^j}\right] = O(hd^{k-2j})\ , \tag{30}$$

if $k \leq 2j+3$. For larger values of k, a generic error term $O(h^4)$ needs to be added to the right hand side.

4.3. Logarithmic terms

The logarithmic terms H_{0k} are treated similarly, but a few further details are needed. For $k = 0$ we rewrite

$$H_{00}(\alpha) = \log(d^2+\hat\alpha^2) = \underbrace{\log(1+\hat\alpha^2)}_{H^u_{00}} + \underbrace{\log\left(\frac{d^2+\hat\alpha^2}{1+\hat\alpha^2}\right)}_{H^b_{00}}\ , \tag{31}$$

where the first term, H^u_{00}, is independent of d and captures the unbounded behaviour of H, while the second term, H^b_{00}, is bounded, with maximum value $|H^b_{00}|_{max} = 2\log d$, and approaches 0 as $\alpha \to \pm\infty$. Although

$H^b = H^b_{00}$ is not self-similar, it is approximately self-similar. For example $H^b = H^b_{max}/4$ when $\alpha \approx \pm d^{1/4}$, as indicated in figure 22(a). The same arguments as before therefore apply and result in a bound for the second term in (31), $E[H^b_{00}] \approx h \log(d^2) = O(h \log d)$. The first term is regular and is integrated to $O(h^4)$ by T_4. The logarithmic term dominates the total error, so

$$E_4[\,\log(d^2 + \hat{\alpha}^2)\,] = O(h \log d)\ . \tag{32}$$

The bounded term H^b_{00}, and the *total* scaled error $E[H_{00}]$ for a range of values a, d, h are plotted in figures 22(a,d), showing results consistent with the arguments just made.

For $k \geq 1$, we rewrite H_{0k} as in the following examples:

$$H_{01}(\alpha) = \ \hat{\alpha}\log(d^2+\hat{\alpha}^2) \ = \hat{\alpha}\log(\hat{\alpha}^2) \qquad\qquad + d\,[\ u\log(1+1/u^2)\,]\ , \tag{33a}$$

$$H_{02}(\alpha) = \hat{\alpha}^2\log(d^2+\hat{\alpha}^2) \ = \hat{\alpha}^2\log(\hat{\alpha}^2) + d^2 \qquad + d^2[u^2\log(1+1/u^2) - 1]\ , \tag{33b}$$

$$H_{03}(\alpha) = \hat{\alpha}^3\log(d^2+\hat{\alpha}^2) \ = \hat{\alpha}^3\log(\hat{\alpha}^2) + d^2\hat{\alpha} \qquad + d^3[u^3\log(1+1/u^2) - u]\ , \tag{33c}$$

$$H_{04}(\alpha) = \hat{\alpha}^4\log(d^2+\hat{\alpha}^2) = \underbrace{\hat{\alpha}^4\log(\hat{\alpha}^2)}_{H^u_{0k}} + \underbrace{[d^2\hat{\alpha}^2 - d^4/2]}_{H^p_{0k}} + \underbrace{d^4[u^4\log(1+1/u^2) - u^2 + 1/2)]}_{H^b_{0k}}, \tag{33d}$$

where $u = \hat{\alpha}/d$. Here, the last term, the bounded term H^b_{0k}, is self-similar, and approaches 0 as $\alpha \to \pm\infty$. It is obtained by subtracting a polynomial H^p_{0k}, given by the middle term, that describes the asymptotic behavior of the logarithmic term. The asymptotic polynomial can be found for any k using Taylor expansions of $\log(1 + 1/u^2)$ as $u \to \pm\infty$. The first term is unbounded and independent of d.

The bounded self-similar term has maximum $|H^b_{0k}|_{max} = O(d^k)$ and thus, by the same arguments as above,

$$E[H^b_{0k}] = O(hd^k)\ . \tag{34}$$

The middle term is a polynomial integrated exactly by T_4 for all degrees ≤ 3. The first term however dominates the integration error. First, we note that the results of Sidi and Israeli Sidi and Israeli (1988) for functions of the form $\hat{\alpha}^k \log \hat{\alpha}^2$ do not apply here, since their results assume that the logarithmic singularity at α_p falls on a gridpoint, which is not the case here. Instead we treat the first term as follows:

$$E_4[\hat{\alpha}^k\log(\hat{\alpha}^2)] = h^k E_{4,I}[(\hat{\alpha}/h)^k\log(\hat{\alpha}/h)^2] + E_4[\hat{\alpha}^k\log h^2] = h^{k+1}E_{4,I/h}[u^k\log u^2] = O(h^{k+1}) \tag{35}$$

for $k \leq 3$. The result (35) follows by a change of variables $u = \hat{\alpha}/h$ since the interval I is proportional to h. We also used the fact that the polynomial $\hat{\alpha}^k \log h^2$ is integrated exactly for $k \leq 3$. For $k > 3$, this term leads to an additional $O(h^4 \log h)$ term that needs to be added to the total error.

The arguments above show that for $k > 0$

$$E_4[\,\hat{\alpha}^k\log(d^2+\hat{\alpha}^2)\,] = O(h^{k+1}, h^4\log h)\ . \tag{36}$$

The scaled bounded components H^b_{0k}, $k = 1, 2$, and the total scaled error $E_4[H_{0k}]$ for a range of values a, d, h are plotted in figures 22(b-c,e-f), showing consistency with the arguments just made.

This completes the derivation of equation (12) and thereby of the convergence of the method presented in §2.4.

5. Summary

This paper presents a method to evaluate boundary integrals of the types given in (1), in the case when the target point $\mathbf{x}_0$ is not on the boundary but at a small distance d from it. These are the types of integrals that describe the solution of elliptic boundary value problems. In particular, they arise in vortex sheet flow and interfacial Stokes flow, in either planar or axisymmetric geometries. The integrals are near-singular when d is small and are difficult to compute accurately with standard quadrature rules.

The proposed method consists of approximating the integrands G by a function $\mathcal{H}$ that captures the near-singular behaviour and can be integrated exactly. The approximation is obtained by truncating a Taylor series expansions of the integrand about a basepoint on the domain boundary. The truncation consists of a

sum of basis functions H_{jk}. The numerical method amounts to adding a correction $E[H_{jk}]$ for each of the basis functions to the trapezoid approximation $T_4[G]$ of the original integral. Analytical bounds are obtained for the integration error of each basis function. These bounds determine the number of corrections required for the desired order of accuracy.

Two versions of the method, of order $O(hd, h^4)$ and $O(hd^2, h^4)$, respectively, are listed explicitly, where d is the distance of the target point to the boundary and h is the meshsize used for the underlying trapezoid rule. The resulting integration error in each case decreases as $d \to 0$ and has maximum value at a distance $d \sim h$ from the boundary that is of order $O(h^2)$ and $O(h^3)$ respectively. The methods were applied to two examples of planar vortex sheet flow consisting of potential flow past a plate and past two cylinders. Convergence of the numerical results at the analytically predicted rates is confirmed. The method was also used to resolve long-term simulation of vortex sheet separation past a plate. The method is conceptually simple and simple to implement, with a cost of $O(n_w)$ operations per target point, where typically $n_w = 10 - 40$, and is presented here as a valuable alternative to resolve near-singular integrals.

All code used to obtain the results presented is available from the author on reasonable request.

Acknowledgments. The author thanks Robert Krasny for many discussions and helpful suggestions, and the anonymous reviewers for their supportive and constructive comments.

A. Positivity of c^2

This section shows that the quantity

$$c^2 = |\dot{\mathbf{x}}_p|^2 + \ddot{\mathbf{x}}_p \cdot (\mathbf{x}_p - \mathbf{x}_0) \tag{37}$$

is positive in the cases considered in this paper, namely a flat boundary with nonuniform point distribution and curved boundaries with equally spaced points. For curved boundaries with target points on the "inside", defined below, d must be sufficiently small.

In the flat case, see figure 23(a), $\ddot{\mathbf{x}}_p$ is tangent to the plate while $\mathbf{x}_p - \mathbf{x}_0$ is normal to it, thus $\ddot{\mathbf{x}}_p \cdot (\mathbf{x}_p - \mathbf{x}_0) = 0$ and

$$c^2 = |\dot{\mathbf{x}}_p|^2 > 0 \tag{38}$$

for all d, and $\mathbf{x}_p$ in the plate interior.

In the equally spaced case, $|\dot{\mathbf{x}}_p| = s_\alpha = constant$, where s is arclength and $s_\alpha = ds/d\alpha$. We consider two possibilities: either $\mathbf{x}_0$ lies on the "outside" of the curve, as in figure 23(b), or $\mathbf{x}_0$ lies on the "inside" of the curve, as in figure 23(c). Here, the "outside" is defined as the side opposite to that pointed into by the normal vector $\mathbf{N}$ at $\mathbf{x}_p$, where

$$\mathbf{N} = \frac{1}{\kappa}\frac{d\mathbf{T}}{ds}\,, \quad \mathbf{T} = \frac{d\mathbf{x}}{ds}\,, \tag{39}$$

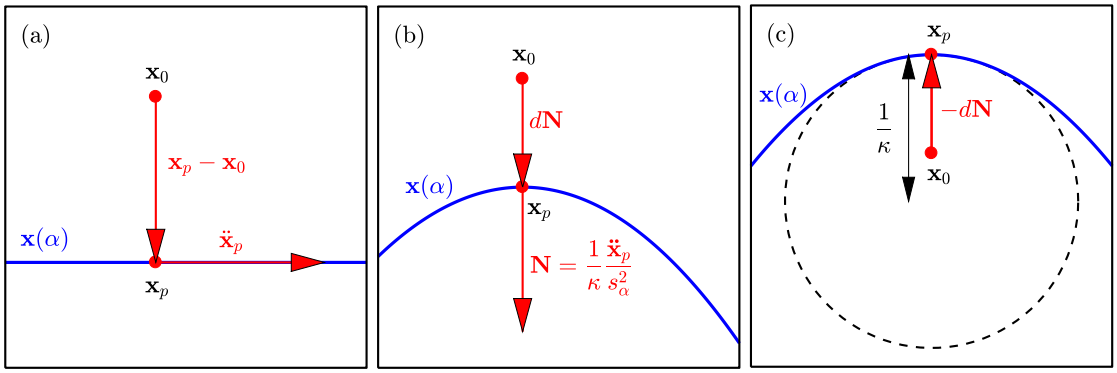

Figure 23. Sketch showing different scenarious: (a) flat curve, and (b,c) uniform arclength parametrization, s_α =constant, with $\mathbf{x}_0$ outside of the curve in (b) and inside of the curve in (c).

while the "inside" is the side containing the osculating circle of the curve at $\mathbf{x}_p$. Here, $\kappa = |d\mathbf{T}/ds|$ is the curvature at $\mathbf{x}_p$. Note that in the equally spaced case,

$$\mathbf{T} = \frac{\dot{\mathbf{x}}_p}{s_\alpha} \ , \quad \mathbf{N} = \frac{d\mathbf{T}}{ds} \Big/ \left| \frac{d\mathbf{T}}{ds} \right| = \frac{1}{\kappa} \frac{\ddot{\mathbf{x}}_p}{s_\alpha^2} \ . \tag{40}$$

Thus if $\mathbf{x}_0$ is on the outside, $\mathbf{x}_p - \mathbf{x}_0 = d\mathbf{N}$ and $\ddot{\mathbf{x}}_p \cdot (\mathbf{x}_p - \mathbf{x}_0) = d\kappa s_\alpha^2 > 0$ so

$$c^2 = s_\alpha^2(1 + d\kappa) > s_\alpha^2 = |\dot{\mathbf{x}}_p|^2 > 0 \ , \tag{41}$$

for all d. If $\mathbf{x}_0$ is on the inside, $\mathbf{x} - \mathbf{x}_0 = -d\mathbf{N}$ and $\ddot{\mathbf{x}}_p \cdot (\mathbf{x}_p - \mathbf{x}_0) = -d\kappa s_\alpha^2$. Therefore

$$c^2 = s_\alpha^2(1 - d\kappa) > \frac{1}{2} s_\alpha^2 = \frac{1}{2} |\dot{\mathbf{x}}_p|^2 > 0 \ , \tag{42}$$

provided $d < 1/(2\kappa) = R_{osc}/2$, where $R_{osc} = 1/\kappa$ is the radius of the osculating circle.

References

Alben, S. (2015). Flag flutter in inviscid channel flow. Phys. Fluids **27**, 033603.

Barnett, A., Wu, B., and Veerapaneni, S. (2015). Spectrally accurate quadratures for evaluation of layer potentials close to the boundary for the 2d Stokes and Laplace equations. SIAM J. Sci. Comput. **37** (4), 519–542.

Barnett, A.H. (2014). Evaluation of layer potentials close to the boundary for Laplace and Helmholtz problems on analytic planar domains. SIAM J. Sci. Comput. **36** (2), A427–A451.

Beale, J. T. and Lai, M-C. (2001). A method for computing nearly singular integrals. SIAM J. Numer. Anal. **38** (6), 1902–1925.

Beale, J. T., Ying, W. and Wilson, J. R. (2016). A simple method for computing singular or nearly singular integrals on closed surfaces. Comm. Comput. Phys. **20**, 733–753.

Carvalho, C., Khatri, S. and Kim, A. D. (2018). Asymptotic analysis for close evaluation of layer potentials. J. Comp. Phys., **355**, 327–341.

Cortez, R. (2001). The method of regularized Stokeslets. SIAM J. Sci. Comput. **23** (4), 1204–1225.

Crowdy, D. and Marshall, J. (2005). On the motion of a point vortex around multiple circular islands. Phys. Fluids, **17**, 056602.

Darakananda, D., de Castro da Silva, A. F., Colonius, T. and Eldredge, J. D. (2018). Data-assimilated low-order modeling of separated flows. Phys Rev Fluids, **3**, 124701.

Elling, V. W. (2020). Vortex cusps. J. Fluid Mech. **882**, A17. doi:10.1017/jfm.2019.827.

Epstein, C. L., Greengard, L. and Klöckner, A. (2013). On the convergence of local expansions of layer potentials. SIAM J. Numer. Anal. **51** (5), 2660-–2679.

Helsing, J. and Ojala, R. (2008). On the evaluation of layer potentials close to their sources. J. Comp. Phys. **227**, 2899–2921.

Huan, Y., Nitsche, M. and Kanso, E. (2015). Stability versus maneuverability in hovering flight. Phys. Fluids **27** (6), 061706.

Huan, Y., Nitsche, M. and Kanso, E. (2016). Hovering in oscillatory flows. J. Fluids Mech. **804**, 531–549.

Jones, M. (2003). The separated flow of an inviscid fluid around a moving flat plate. J. Fluid Mech **496**, 405–441.

Jones, M. and Shelley, M. J. (2005). Falling cards. J. Fluid Mech **540**, 393–425.

Khatri, S., Kim, A. D., Cortez, R. and Carvalho, C. (2020). Close evaluation of layer potentials in three dimensions. J. Comp. Phys. **423**, 109798.

Klinteberg, L. af and Tornberg, A.-K., (2016). A fast integral equation method for solid particles in viscous flow using quadrature by expansion. J. Comp. Phys. **326**, 420–445.

Klinteberg, L. af and Tornberg, A.-K., (2017). Error estimation for quadrature by expansion in layer potential evaluation. Adv. Comput. Math. **43**, 195–234.

Klinteberg, L. af and Tornberg, A.-K., (2018). Adaptive quadrature by expansion for layer potential evaluation in two dimensions. SIAM J. Sci. Comp. **40** (3), A1225–A1249.

Klöckner, A., Barnett, A., Greengard, L. and O'Neil, M. (2013). Quadrature by expansion: A new method for the evaluation of layer potentials. J. Comp. Phys. **252**, 332–349.

Mayo, A. (1985). Fast high order accurate solution of Laplace's equation on irregular regions. SIAM J. Sci. Statist. Comput. **6**, 144–157.

Nitsche, M. (1996). Scaling properties of vortex ring formation at a circular tube opening. Phys. Fluids **8** (7), 1848–1855.

Nitsche, M. (1999). Axisymmetric vortex sheet motion: accurate evaluation of the principal value integrals. SIAM J. Sci. Comput. **21** (3), 1066–1084.

Nitsche, M. (2001). Singularity formation in a cylindrical and a spherical vortex sheet. J. Comput Phys. **173** (1), 208–230.

Nitsche, M., Ceniceros, H. D., Karniala, A. L. and Naderi, S. (2010). High order quadratures for the evaluation of interfacial velocities in axi-symmetric Stokes flows. J. Comp. Phys. **229**, 6318–6342.

Nitsche, M. and Krasny, R. (1994). A numerical study of vortex ring formation at the edge of a circular tube. J. Fluid Mech. **276**, 139–161.

Ojala, R. and Tornberg, A.-K. (2015). An accurate integral equation method for simulating multi-phase Stokes flow. J. Comp. Phys. **298**, 145–160.

Pérez-Arancibia, C., Faria, L. M. and Turc, C. (2019). Harmonic density interpolation methods for high-order evaluation of Laplace layer potentials in 2D and 3D. Journal of Computational Physics **376**, 411–434.

Quaife, B. Biros, G. (2014). High-volume fraction simulations of two-dimensional vesicle suspensions. J Comp Phys **274** (1), 245–267.

Rahimian, A., Barnett, A. and Zorin, D. (2018). Ubiquitous evaluation of layer potentials using quadrature by kernel-independent expansion. BIT Numerical Mathematics **58** (2), 423–456.

Sheng, J. X., Ysasi, A., Kolomenskiy, D., Kanso, E., Nitsche, M. and Schneider, K. (2012). Simulating vortex wakes of flapping plates, Natural locomotion in fluids and on surfaces, 255–262.

Shukla R. K. and Eldredge, J. D. (2007). An inviscid model for vortex shedding from a deforming body. Theor. Comput. Fluid Dyn. **21**, 343–368.

Sidi, A. and Israeli, M. (1988). Quadrature methods for periodic singular and weakly singular Fredholm integral equations. J Sci. Comput. **3** (2), 201–231.

Siegel, M. and Tornberg, A.-K. (2018). A local target specific quadrature by expansion method for evaluation of layer potentials in 3D. Michael Siegel and Anna-Karin Tornberg, J. Comp. Phys. **364**, 365–392.

Sohn, S.-I. (2020). An inviscid model of unstead separated vortical flow for a moving plate. Theor. Comput. Fluid Dyn. **34**, 187–213.

Tlupova, S. and Beale, J. T. (2013) Nearly singular integrals in 3D Stokes flow. Comm. Comput Phys. **14**, 1207–1227.

Tlupova, S. and Beale, J. T. (2019) Regularized single and double layer integrals in 3D Stokes flow. J. Comp. Phys. **386**, 568–584.

Xu, L., Nitsche, M. and Krasny, R. (2017). Computation of the starting vortex flow past a flat plate. Procedia IUTAM, **20**, 136–143.

Ying, L., Biros, G. and Zorin, D. (2006). A high-order 3D boundary integral equation solver for elliptic PDEs in smooth domains. J Comp Phys **219** (1) 247–275.